RESEARCH TECHNICAL REPORT

Radiation-Activated Sprinklers

FM Global®

Radiation-Activated Sprinklers

Prepared by

Jaap de Vries

February 2017

FM Global
Norwood, MA 02062

PROJECT ID 0003058376

Disclaimer

The research presented in this report, including any findings and conclusions, is for informational purposes only. Any references to specific products, manufacturers, or contractors do not constitute a recommendation, evaluation or endorsement by Factory Mutual Insurance Company (FM Global) of such products, manufacturers or contractors. FM Global does not address life, safety, or health issues. The recipient of this report must make the decision whether to take any action. FM Global undertakes no duty to any party by providing this report or performing the activities on which it is based. FM Global makes no warranty, express or implied, with respect to any product or process referenced in this report. FM Global assumes no liability by or through the use of any information in this report.

Executive Summary

Conventional sprinklers operate due to convective flow of hot gases past the heat responsive element, which renders them ineffective in situations where hot gases from the fire plume are not in direct contact with the sprinkler. For example, following an ignitable liquid tests with grated mezzanine construction inside FM Global's Large Burn Laboratory, several sprinklers failed to operate even when residing directly adjacent to a significant fire. In one case, a sprinkler pipe immersed in the fire broke without activating attached sprinklers. This test observation identified a need for a radiation-activated sprinkler (RAS).

In this study, a new conceptual sprinkler design is proposed that activates when exposed to external radiation. The business benefit to FM Global of a RAS is to maximize the sprinkler effectiveness in special situations, such as external exposure protection, sprinkler protection beneath grated mezzanines, and protection from other unique fire hazards, such as covered open yard storage. This study is presented in three phases.

In the first phase, the response of conventional, commercially available sprinklers and sprinkler links was measured by exposing them to external radiation. These tests were conducted to provide data and insights into how conventional sprinklers respond to external radiation; how the sprinkler orientation impacts the response time; what heat responsive element type (glass bulb or soldered) fuses faster when exposed to external radiation; and if the heat transfer physics can be modeled effectively.

Quick Response (QR) and Standard Response (SR) sprinklers were tested inside the Small Burn Laboratory at FM Global's Research Campus in West Glocester, RI, USA. The response times of both soldered and glass-bulb sprinklers were measured as a function of external radiation intensities - set between 8 and 21 kW/m^2. Standard response high-temperature-rated (141°C) glass-bulb sprinklers operated slowly and required as much as 16 kW/m^2 to operate. When turned 90° with respect to the incoming radiation, glass-bulb links took longer due to the obstruction of the radiation by the sprinkler arms. In some cases, sprinklers did not operate at all.

In addition to QR and SR sprinklers, individual soldered, quick response (QR) links, removed from their sprinkler housing, were tested using a Fire Propagation Apparatus (FPA). These tests were conducted with uniform heat fluxes ranging between 2 kW/m^2 and 10 kW/m^2. FPA measurements included both the link activation times and surface temperature histories, which were recorded using a long-wave IR camera. A 1-D transient heat transfer model could successfully predict the operating times and temperature histories of these soldered links.

Based on the findings during Phase I, it was concluded that a radiation-activated sprinkler design should (1) contain sprinkler links comprised of soldered thin fusible elements and (2) orient links within a sprinkler to maximize exposure to external radiation from any direction, i.e., optimize the view factor. The knowledge gained during Phase I was used in the design of a new, conceptual, radiation-activated sprinkler.

Phase II focused on the design, development, and testing of two novel radiation-activated sprinkler designs (namely, RAS A and B). During this part of the study, fifty-three sprinkler activation tests were performed. All tests were conducted inside FM Global's Small Burn Laboratory (SBL) in West Glocester, RI, USA.

Both RAS A and B consisted of modified versions of existing, commercially available, residential sprinklers. Both RAS were tested at external radiation levels ranging between 2 kW/m^2 and 11 kW/m^2 using a special test apparatus. The effect of the incoming radiation angle was studied by exposing both sprinklers at 0º and 45º with respect to the centerline of the sprinkler.

The effects of several parameters influencing the radiation-activated sprinkler's performance were tested in a systematic manner. Three RAS design characteristics influencing performance were studied; namely, the emissivity of the heat responsive element, the use of a reflector behind the element, and insulation on the backside (unexposed side) of the element. The effects of these parameters were examined via a full-factorial Design of Experiments (DoE) method.

The experimental results successfully demonstrated the RAS designs. On average, both RAS designs operated between 100 and 16 seconds when exposed to radiant flux levels ranging from 2 kW/m^2 to 11 kW/m^2, respectively. Further testing showed that the high emissivity coating on the heat responsive element had the greatest effect on reducing response times. Placing a reflective mirror behind the element also reduced the activation time significantly. Insulating the backside of the element had a marginal effect on the measured activation time.

In the third and final phase of this study, Phase III, the benefit of the RA sprinkler over conventional, commercially available sprinklers was demonstrated via ten side-by-side tests. In the test setup, the radiant fire source consisted of a 1.0-m diameter heptane pool fire. Both the RA sprinklers and a conventional quick-response (QR), glass-bulb sprinkler were placed at a 3.0 m vertical and 2.0 m horizontal distance on opposite ends from the centerline of the pool fire. On average, the RA sprinklers activated 100 seconds after ignition of the pool fire, while the conventional QR sprinklers failed to operate in all but one instance. A multi-node radiant heat transfer model is used to confirm the estimates of radiant exposure based on measured sprinkler response.

The demonstration tests showed that the RAS concepts implemented in the modified sprinklers performed favorably in situations in the absence of a flow of hot gases past the sprinkler and where the main heat transfer mode was radiation. Therefore, the transfer of technology that leads to the development of commercially available radiation-activated sprinklers is recommended.

Abstract

This report describes the development of a radiation-activated sprinkler (RAS). Conventional sprinklers operate due to convective flow of hot gases, which makes them ineffective in situations where hot ceiling layers are not formed. Since conventional sprinklers are not designed to activate when exposed to just radiation, little scientific data exist on this topic. This work is divided in three phases. In the first phase, the response of both conventional glass-bulb and soldered-link sprinklers to external radiation was investigated at heat fluxes up to 21 kW/m^2. Experiments showed that the orientation of a sprinkler with respect to the incoming radiation has a strong effect on the operating time. In addition to sprinkler tests, individual soldered links - removed from their housing - were tested at heat fluxes ranging between 2 kW/m^2 and 10 kW/m^2. Link surface temperatures were measured using a long-wave infrared camera and compared against a physics-based model. In the second phase, two different radiation-activated sprinklers (RAS A and B) were developed by modifying existing, commercially available, sprinkler designs. The response of these RAS prototypes was measured at heat flux levels ranging between 2 kW/m^2 and 11 kW/m^2. A Design of Experiment (DoE) test methodology was employed to study the effect of high-emissivity coatings, insulation, and reflective mirrors on the response time of these sprinklers. Test results demonstrated successful operation of the two radiation-activated sprinklers. In the final phase, Phase III, the response of both RAS A and B was measured by exposing them to a 1-meter diameter heptane pool fire. These side-by-side test results demonstrated that the newly designed and developed RAS consistently activated under 100 seconds. The conventional QR sprinkler failed to activate in all but one test. Finally, a multi-node radiant heat transfer model is used to confirm the estimates of radiant exposure obtained from sprinkler response measurements.

Acknowledgements

Table of Contents

List of Figures

List of Tables

PAGE LEFT INTENTIONALLY BLANK

1. Introduction

1.1 Radiation-Activated Sprinkler Concept

Conventional sprinklers operate due to heating of the heat responsive element to predetermined temperature ratings. In most sprinkler applications, especially when installed under a ceiling, hot gases in the ceiling layer pass the sprinkler heat responsive element so that convection is the dominant mode of heat transfer. This renders traditional ceiling sprinklers ineffective in situations where hot ceiling layers are absent. For example, following an ignitable liquid tests using grated mezzanine construction inside the Large Burn Laboratory on FM Global Research Campus at West Glocester, RI, USA, several sprinklers failed to operate even though they were adjacent to a significant fire. In one case, a sprinkler pipe immersed in the fire broke without activation of the attached sprinklers. This test observation highlighted the need for a radiation-activated sprinkler (RAS).

The RAS could be beneficial for sprinkler installed on vertical walls or below grated mezzanines often used in chemical plants and the oil and gas industry. In these cases, the sprinklers are not subjected to a hot ceiling layer, (see Fig. 1-1). Therefore, radiation heat transfer can be utilized to achieve sprinkler activation.

Figure   1-1:   Ethanol pool fire underneath a two-level grated mezzanine [1].

A RAS could provide protection options where currently none exist; improve the performance of protection FM Global presently recommends; and be a catalyst for new applications where convection-operated sprinklers have historically not been applied.

1.2   Potential Applications

Current sprinkler design is mainly aimed at under-ceiling or inside storage racks applications, where the heat responsive element is activated via convective heat transfer. To ensure prompt activation of a sprinkler, the element should be located below a solid surface or at other position that forces the flow of hot gas past it. In the absence of proximity to a hot gas flow, the main mode of heat transfer becomes radiation, unless a sprinkler is placed very close to the axis of the fire source. The difference in heat transfer modes is depicted in Fig. 1-2 using a ceiling installation as an example.
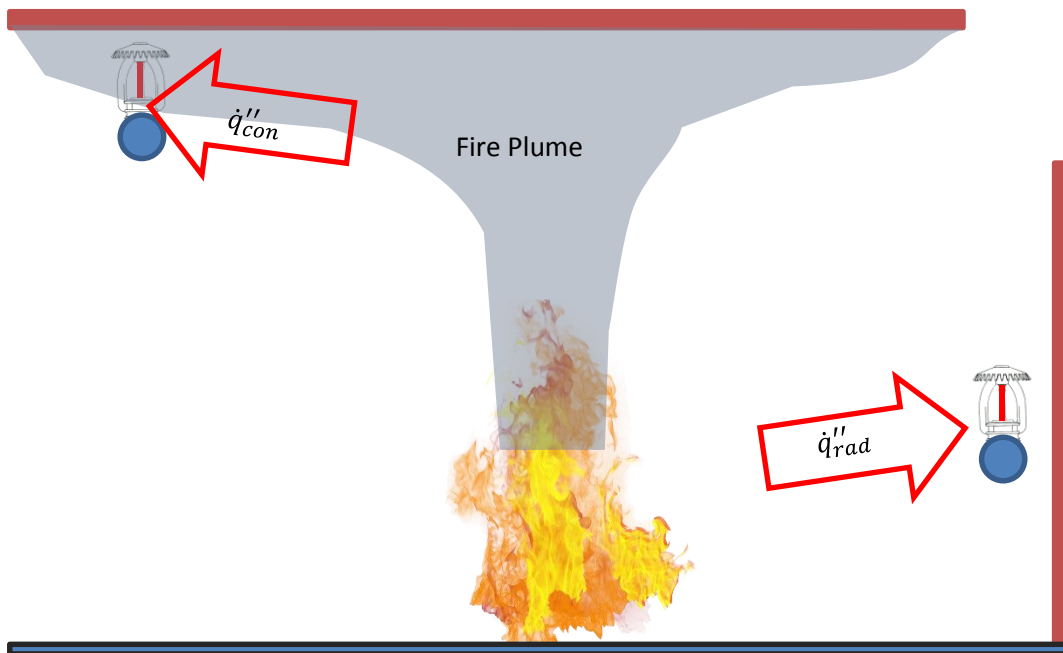
Figure   1-2:   Difference between a sprinkler activation via convective heat transfer from the fire plume or ceiling layer (left top) and a sprinkler activated via radiation (right).

While for many storage situations conventional ceiling sprinklers can provide adequate protection, there are scenarios where sprinklers could be installed in locations that are not swept by a hot ceiling layer. The following three hazard cases represent examples of potentially significant exposures:

- External exposure sprinkler protection.
- Sprinkler protection beneath grated mezzanines.
- Special hazard sprinkler protection (*e.g.,* sprinklers not located below a ceiling).

1.2.1 External Exposure Sprinkler Protection

Sprinklers in external exposure applications are installed on vertical outside walls or windows to protect the building against an external fire source. This protection approach is accomplished using either a deluge sprinkler installation or by installing standard closed sprinklers on a wet or dry sprinkler system. Unless the fire exposure originates directly underneath the sprinkler, these sprinklers would rely predominantly on radiation to activate. The development of a RAS or heat detector would provide a means of achieving the protection goal for exposure protection (i.e., timely delivery of a spray of water on the wall or window to prevent ignition of the building or its contents from an external fire exposure).

1.2.2 Grated Mezzanine Protection

Grated mezzanines are commonly found in many industrial facilities. Combustibles are often present above and below the mezzanine. They can be in warehouses, industrial facilities such as chemical plants, power generation facilities, or manufacturing facilities. Historically, sprinklers are placed below the mezzanine; however, their effectiveness is not always certain. It is probable that only sprinklers directly exposed to fire will operate.

If the protection below the mezzanine is critical, the new version of FM Global's Loss Prevention Data Sheet 2-0, *Installation Guidelines for Automatic Sprinklers* (DS 2-0) [2], recommends using a reduced sprinkler spacing (1.2 m x 1.2 m) which increases installation costs.

The use of radiation activating sprinklers below grated mezzanines could ensure prompt activation of nearby sprinklers, which will improve fire control and reduce the number of sprinklers that will operate at the ceiling [2].

1.2.3 Special Hazard Sprinkler Protection

Finally, a RAS would be beneficial in cases where sprinkler protection is needed away from the ceiling, for instance to protect unique arrangements of combustible materials or building interior features. The sprinkler could be located in free space above the protected hazard. This type of application includes lubrication oil systems, shielded areas within and beneath equipment (presses), rack arrangements that do not allow the installation of in-rack sprinklers, water curtains protecting building walls and floor openings, and protection of combustible wall panels. As an example of special protection, Fig. 1-3 shows a sprinkler located in the middle of the aisle protecting spiral separators which are commonly found in mining operations.

1.3 Report Structure and Technical Approach

The objective of this study is to demonstrate the concept of a RAS. The technical approach was to test and analyze the response of existing, commercially available sprinklers to external radiation, followed by suggested physical design changes that can improve performance in a thermal radiation environment.

The remainder of this report describes three major research tasks. Chapter 2 investigates the response of conventional, commercially available sprinklers. Chapter 3 describes the development and characteristics of two proof-of-concept RASs. These RASs were created by modifying commercially available sprinkler designs. In Chapter 4, the effectiveness of the newly developed RASs is demonstrated

by exposing them to a pool fire. Finally, a summary of the results and the conclusions drawn from this study are presented in Chapter 5.

Figure   1-3:   Example of protection for spiral separators in a mining operation. The sprinklers are hung in the middle of the aisle.

2. Sprinkler Response to Radiation

2.1 Convectional Sprinkler Response

The response of conventional, commercially available sprinklers to convective heat transfer is well studied. In fact, measuring the response time of a sprinkler submerged into a wind tunnel supplying heated air is part of FM Global's sprinkler certification process by FM Approvals. How conventional sprinkler respond when exposed to external radiation has not been studied. For clarity, the term "conventional sprinklers" here refers to commercially available sprinkler assemblies intended to be installed below a solid ceiling and which are approved by means of a hot gas flow (plunge tunnel test). This section describes a series of tests conducted to study the activation times of three conventional sprinkler types subject to radiation fluxes.

2.1.1 Sprinklers Tested

Three sprinklers representing a broad range of conventional sprinklers were selected for testing. These three sprinklers are referred to as Sprinkler A, B, and C. Sprinkler A and B are both Quick Response (QR) sprinklers with a temperature rating of 74ºC and 68ºC, respectively. Sprinkler C is a Standard Response (SR) sprinkler with a temperature rating of 141ºC. Further properties and specifications of these sprinklers are presented in Table 2-1.

Table   2-1:   Properties of tested conventional sprinklers.

Name	Sprinkler A	Sprinkler B	Sprinkler C
Orientation	pendent	pendent	pendent
Temperature ºC	74	68	141
Discharge coefficient (K-factor), lpm/bar$^{1/2}$	360	160	160
Nominal Response Time Index (RTI), m$^{1/2}$s$^{1/2}$	24	63	153
Heat responsive element	soldered	bulb	bulb
Bulb liquid	N.A.	red	blue
Response type	QR	QR	SR

2.1.2 Test Setup

The response times of commercially available sprinkler to external radiant heat fluxes were measured from multiple angles. All activation tests were performed inside the Small Burn Laboratory (SBL) at FM Global's Research Campus, located in West Glocester, RI, USA. The test setup consisted of a propane-fed, radiant burner (Detroit Radiant, Model DR-160) providing external heat flux levels up to 30 kW/m². The radiant panel was placed on a movable stand and the intensity of the external radiation was controlled by changing the distance between the panel and the sprinkler link. For these tests, each sprinkler was attached to a pressurized tube and placed behind an aluminum panel with a window cut-

out. A plate covering the window was allowed to slide up and down and held up via a string and pulley mechanism. This hatch-style window cover allowed for a distinct start time of the onset of radiant exposure to the sprinkler. A picture of the test setup is shown in Fig. 2-1.

(a)   (b)
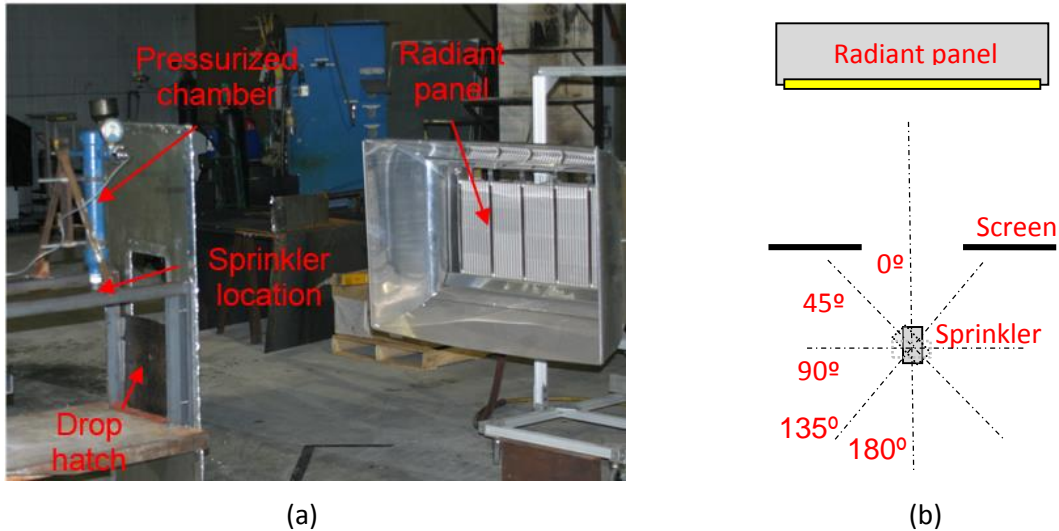
Figure   2-1: Test setup showing the pressurized chamber and the radiant panel (a). Plan view of the test showing the view angles with respect to the front of the sprinkler used (b).

The pressure inside the main tube was monitored via an electronic pressure transducer. In addition, a Bourdon gauge (0-6 bar) was attached to the tube providing a visual pressure reading. Sprinkler activation times were defined as the interval from the drop of the plate in front of the window to the rapid pressure decrease inside the tube. A graphical depiction of this process is shown in Fig. 2-2. Initially, the tube was pressurized to 1.5 bar. The time of sprinkler activation is clearly shown in the pressure-time history. Each sprinkler was tested starting with the sprinkler frame arms parallel to the radiant panel (0°) and was then rotated along its vertical axis. Such test design helped quantify the blocking effect of the sprinkler arms so that differences in view factor could be established.
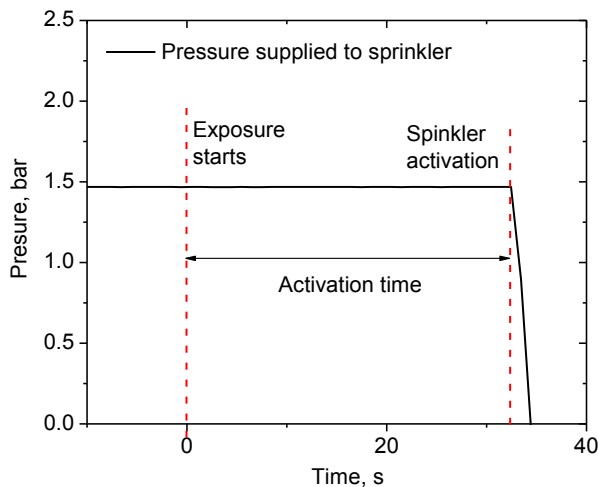
Figure   2-2: Pressure history during a sprinkler activation test.

2.1.3 Heat Flux Calibration

Prior to sprinkler testing, a calibration procedure was performed to determine the relationship between the radiant heat flux level at the sprinkler location and panel distance. For this calibration, a water-cooled, Schmidt-Boulter type (0-100 kW/m²) heat flux gauge was placed at the sprinkler location [see Fig. 2-3(a)]. For the calibration established in this study, the distance between the radiant panel and the heat flux gauge was varied between 274 cm and 53 cm, resulting in measured heat fluxes ranging from 1.5 kW/m² to 21 kW/m², respectively. The result of the heat flux calibration is shown in Fig. 2-3(b). The measured data were fitted using a first order exponential decay function of the form

$$\dot{q}'' = 38.1 \, exp\left(-\frac{x}{75.0}\right) \tag{2-1}$$

where $\dot{q}''$ is the measured radiant heat flux in kW/m² and x is the distance in cm between the radiant panel and the heat responsive element. Equation (2-1) fits the data with an adjusted R-squared of 0.98. Once the calibration was established, the desired heat flux levels could be obtained by solving Eq. (2-1) for x, given a desired heat flux.
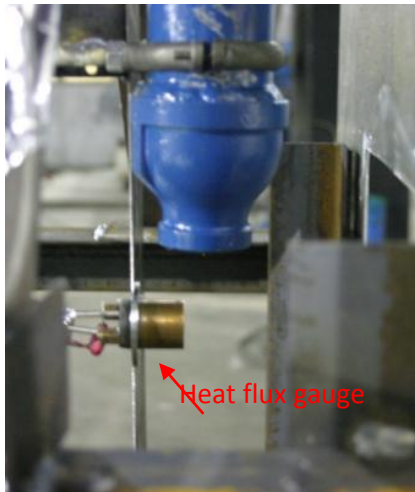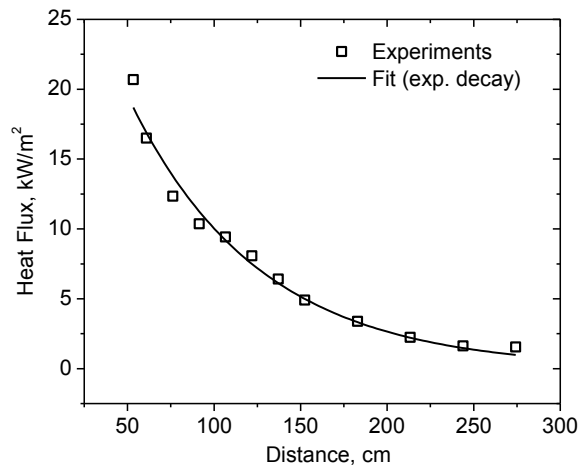
(a)   (b)

Figure   2-3:   Location of heat flux gauge during the calibration test (a). Effect of separation distance on measured heat flux (b).

2.1.4 Test Results

Sixty-four sprinkler activation tests were conducted inside the SBL. The first forty tests were conducted using Sprinkler A (Soldered link, QR, 74°C). The remaining twenty-four tests were conducted using Sprinkler B (glass bulb link, QR, 68°C) or Sprinkler C (glass bulb link, SR, 141°C). The maximum test duration was set to 10 minutes. If the sprinkler did not activate within ten minutes, the test was terminated.

Sprinkler A was tested at different orientations between 0 and 180º in 45º intervals (i.e., 0º, 45º, 90º, 135º, 180º). Figure 2-4 shows a plot of the measured sprinkler activation time vs radiant heat flux. Note that, when the sprinkler arm blocks radiation, the activation time can exceed several minutes.
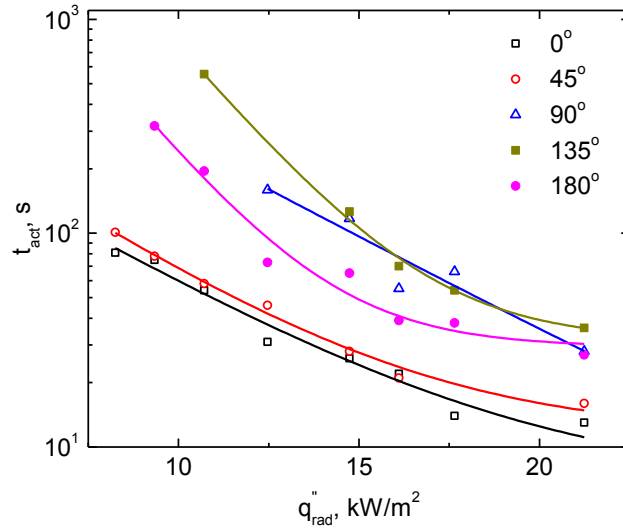
Figure   2-4:   Sprinkler activation time of Sprinkler A with radiation angles ranging from 0º to 180º.

Sprinkler B was tested at two different orientations, namely at 0 and 90º. Figure 2-5 shows a plot of the measured sprinkler activation time vs radiant heat flux. Note that, when the sprinkler arm is blocking radiation, the activation time can be in excess of several minutes. Figure 2-6 shows the activation times for a SR, high temperature rated sprinkler. Below 16 kW/m^2 sprinkler C would not activate within 10 minutes.
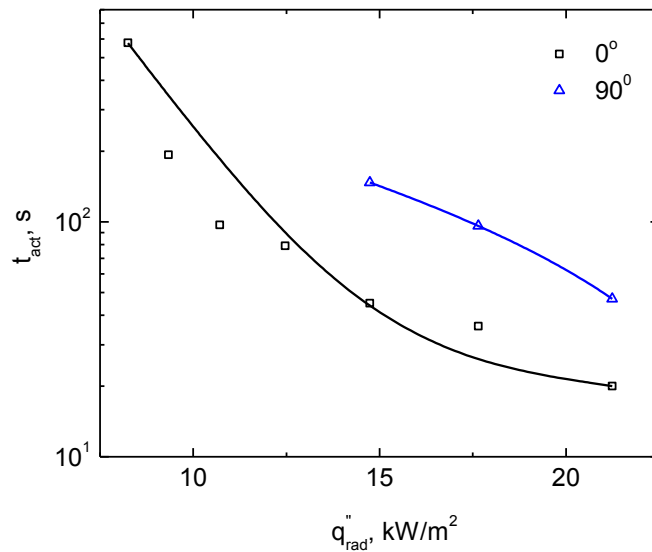
Figure   2-5:   Sprinkler activation time of Sprinkler B with radiation angles at either 0º or 90º.
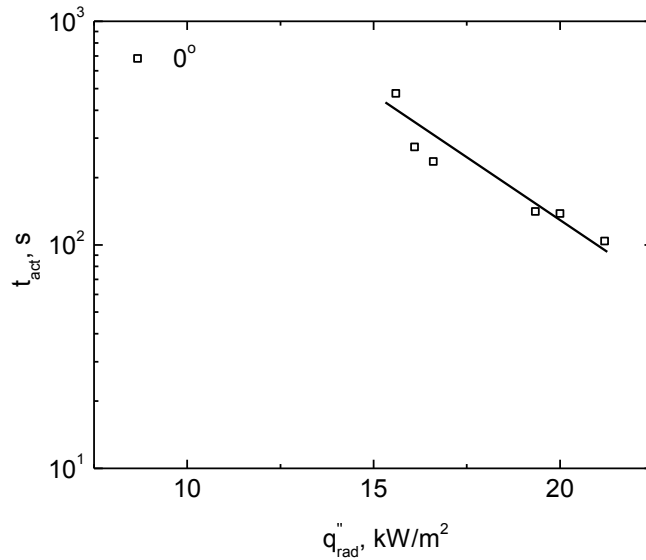
Figure   2-6:   Sprinkler activation time of Sprinkler C with a radiation angle of 0º.

2.2   Sprinkler Link Analysis

In most instances, soldered links have a smaller Response Time Index (RTI) and better surface to volume ratios compared to glass bulb links. Therefore, they are more suitable to be used in RAS designs. To investigate their performance in greater detail, individual soldered links were removed from their sprinkler housing and tested by exposing them to predetermined external radiation.

2.2.1   Test Setup

Individual links of the Sprinkler A were tested using a Fire Propagation Apparatus (FPA) located inside the Flammability Lab at the FM Global Center for Property Risk Solutions in Norwood, MA. Both the time-till-breakage and the surface temperatures were recorded. A general schematic of the FPA is shown in Fig. 2-7. A complete description of the FPA can be found in Refs. [3] and [4].

During these tests, individual fusible elements were tensioned and placed on a spring-loaded holder. The holder was protected by an insulating ceramic blanket (Cotronics Corp., 370-series). This material is made from asbestos free, high purity refractory fibers that are resistant to oxidizing and reducing atmospheres, molten non-ferrous metals, steam, most chemicals and solvents. An image of the holder is shown in Fig. 2-8(a). The springs were set to a loading of 50 N. The initial tension placed on the link had little effect on the fusing time. The holder was placed inside the FPA. Once the link holder was in place, an IR camera was positioned on top of the quartz tube facing down towards the sprinkler link. The complete experimental setup is shown in Fig. 2-8 (b).
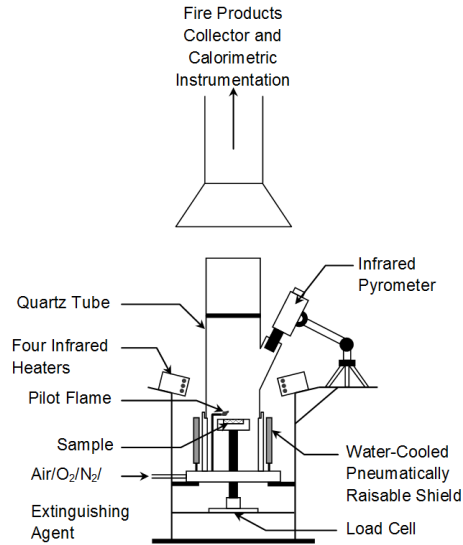
Figure   2-7:   Schematic of the Fire Propagation Apparatus (FPA).
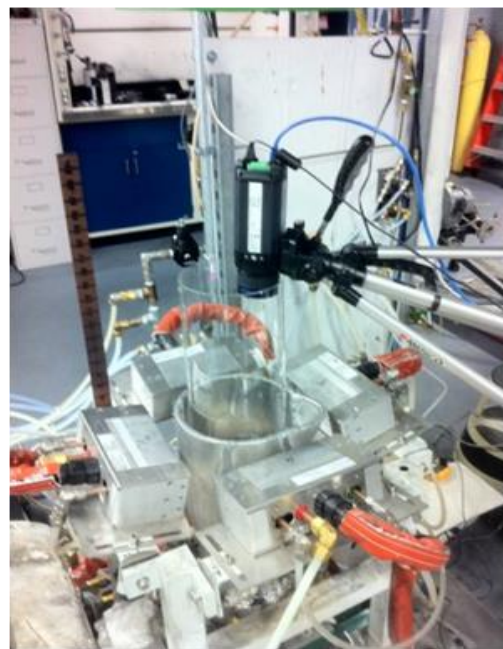
(a)   (b)

Figure   2-8:   Spring loaded sprinkler element holder (a). Sprinkler element holder placed inside the FPA with the SC655 IR camera positioned on top of the quartz tube (b).

An infrared (IR) camera (model FLIR® SC655) was used to monitor the link's surface temperature during each test. This model camera uses an uncooled, high-resolution 640 x 480, 17-μm (6.7 10^{-4}-in.) pixel detector. Detailed specifications are given in Reference [5]. Pixel depth is 14 bit and the thermal sensitivity is 0.05°C @ 30°C with a Noise Equivalent Temperature Difference (NETD) of 50 mK. The spectral range of the camera is 7.5-13 μm.

The surface emissivities of the fusible elements were measured in a separate calibration procedure involving a fusible element and a surface mounted thermocouple. Surface emissivities were measured at temperatures ranging between 20 and 150 ℃. The average value was found to be 0.867± 0.013. This emissivity value was used to determine the surface temperature during all FPA tests. The emissivity was found to be temperature independent within the tested range.

Figures 2-9(a)-(d) show four IR images taken 2, 8, 13, and 20 seconds after radiation exposure for a link exposed to a calibrated heat flux of 8.0 kW/m^2. The associated temperatures are plotted on the right of each image. The black line represents a physics based 1-D heat transfer model of the link, which is described in greater detail in Section 2.2.3. The red line represents the measured temperature using the IR camera. After 17 seconds, the link fuses causing a drop in the measured temperature.

(a)

(b)

(c)

(d)
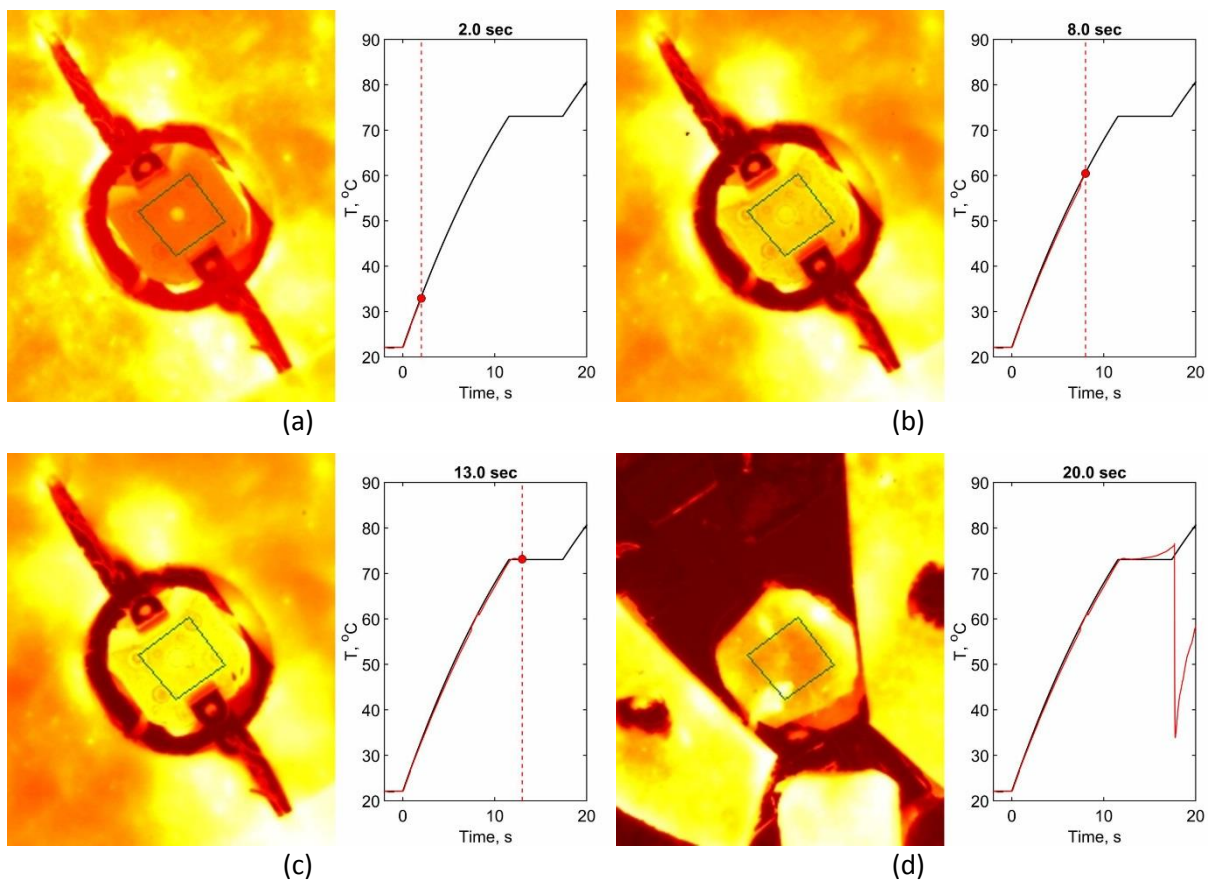
Figure 2-9: IR images and associated average temperatures within the region of interest (green rhombus) of a heated link inside the FPA after 2 s (a), 8 s (b), 13 s (c), and 20 s (d) exposure.

2.2.2 Test Results

Nine tests were conducted in the Fire Propagation Apparatus (FPA). Using the emissivity found from the calibration procedure, link temperatures measured using the IR camera could be determined with

reasonable confidence. Two such temperature histories are shown in Fig. 2-10. The red line shows a link exposed to 7 kW/m², while the black line shows the same link exposed to 5 kW/m². Both curves reach the isothermal melting phase near 74°C, which is the temperature rating of the links. The isothermal phase change of the solder requires a set amount of time, after which the link fuses. The link activation time is defined as the time between the onset of external radiation and the fusing of the link.
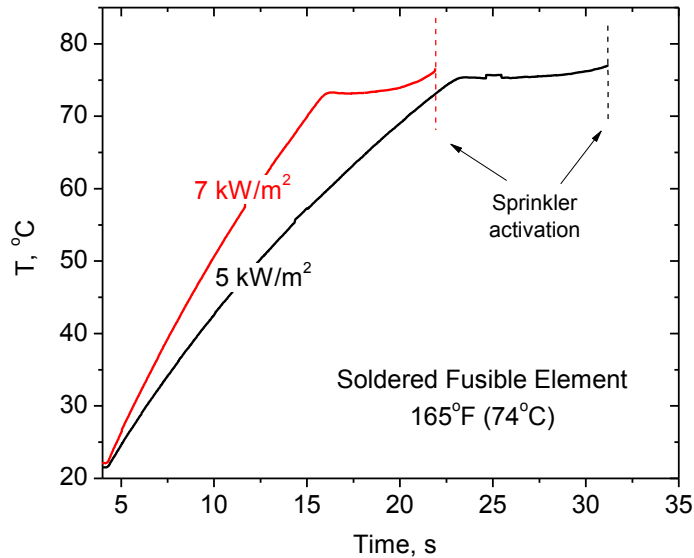
Figure   2-10: Sprinkler link temperature histories measured up to activation by the IR camera.
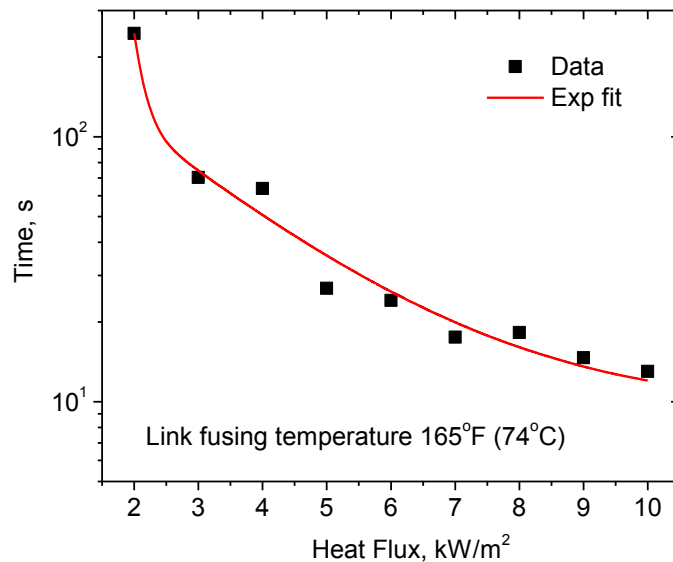
Figure   2-11: Sprinkler link temperature histories measured up to activation by the IR camera.

Link activation times for heat fluxes ranging between 2 and 10 kW/m² are plotted in Fig. 2-11. A fit through the data is also shown in the figure. Note the highly non-linear relationship between the supplied heat flux and the activation time. Under these idealized test conditions, links can activate with

heat fluxes as low as 2 kW/m². Figure 2-12 shows both the test results for the individual links and for the whole sprinkler. The difference in activation time is due to the difference in view factor and to radiation blockage by sprinkler elements.
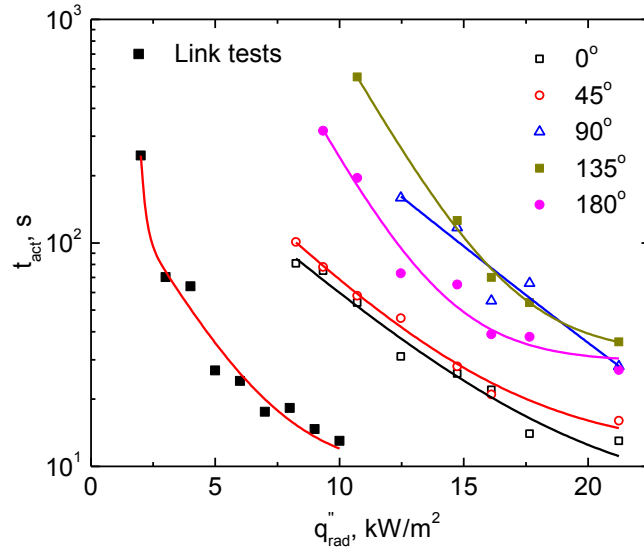
Figure   2-12:   Individual link data compared to sprinkler tests.
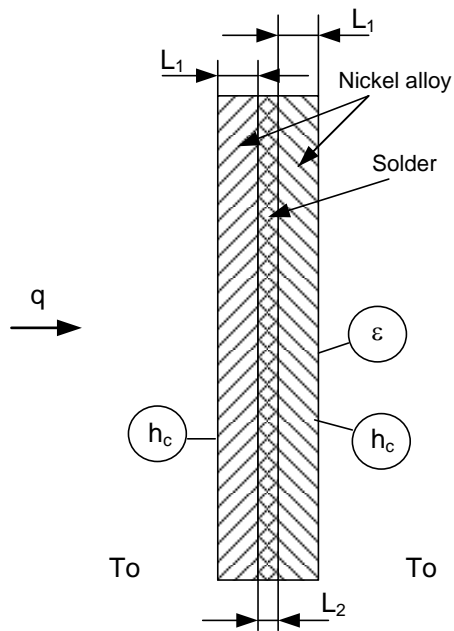
Figure   2-13:   Simple schematic of a RAS link.

2.2.3 Heat Transfer Model for Sprinkler Links

Tests results have shown that quick response soldered links respond faster when exposed to external radiation than standard response or even quick response glass bulbs. Most likely, a RAS design will utilize a soldered fusible link. It is therefore helpful to characterize the activation times of a fusible element based on its properties. In order to do so, one should recognize that the fusing of a soldered link spans two phases; namely, a heating phase, in which the element gets heated to its activation temperature, and an isothermal solder melting phase. Theoretically, the amount of solder required to melt before the sprinkler activates depends on the tension that is initially placed on the sprinkler link; therefore, for the link to break, the following inequality should hold

$$(A_i - A_m)\sigma_s > F_{pre} \tag{2-2}$$

In Eq. (2-2), A_i is the total initial area of the link where there is a soldered connection, A_m is the total area of solder that is melted, σ_s is the shear strength of the solder and F_{pre} is the tension initially placed on the link.

Analysis of a fusible element exposed to radiation can be simplified when making the following assumptions:

- The link is thin and has a low Biot number. The Biot number, $Bi = hL/k$, represents the ratio between the heat transfer resistance inside and at the surface of an object. With low Biot number numbers, the lumped capacity method can be used (no thermal gradients within the solid link material).
- All solder material is required to melt for the link to operate. Technically the tension on the link might cause the link to fuse before all the solder has melted; however, given the shear strength of the solder and the limited tension on the link, this may be a reasonable assumption.
- Convective losses are the same at the front and back of the link.

The link operating time can be derived by separating the heating phase (I) and the melting phase (II). The activation time is therefore, $t_{act} = t_{phase_I} + t_{phase_{II}}$.

Details on the fusible elements used in this analysis are given in Table 2-2. A schematic of the link is shown in Fig. 2-13. Given these properties, the fusing time of the link can be derived analytically as detailed in the following derivation.

The heating of an element can be described by the following heat transfer model

$$A(2\rho_n c_{p,n} L_1 + \rho_s c_{p,s} L_2)\frac{dT_s}{dt} = A\left(\alpha \dot{Q}''_{rad} - \sum \dot{Q}''_{loss}\right) \tag{2-3}$$

In Eq. (2-3), A is the exposed area of the link; ρ_n and ρ_s, $c_{p,n}$ and $c_{p,s}$, and L_1 and L_2 are the densities, specific heats, and thicknesses of the nickel alloy and solder, respectively. T_s is the surface temperature of the link, t is the time. $\dot{Q}''_{rad}$ is the supplied external radiation, α is the link's surface absorptivity, and $\sum \dot{Q}''_{loss}$ is the sum of the heat losses due to convection and radiation.

Table   2-2:   Properties used in fusible soldered link activation time calculations.

Property		Symbol	Value	Unit
Environmental Conditions				
Ambient Temperature		T_{amb}	22	ºC
Initial Temperature		T_{int}	22	ºC
Stefan-Boltzmann Constant		σ	5.67 10^{-8}	W/m^{2}K^4
Convective heat transfer coefficient back		h_b	23	W/m^{2}K
Convective heat transfer coefficient front		h_f	23	W/m^{2}K
Absorptivity Front		α_f	0.876	-
Absorptivity Back		α_b	0.876	-
Thickness nickel layer		L_1	0.127	mm
Thickness solder layer		L_2	0.0635	mm
Material Properties				
Nickel Alloy	Density	ρ_n	8280	kg/m^3
	Specific Heat	c_{p1}	444	J/kg-K
	Thermal Conductivity	k_n	48	W/m-K
Indalloy 158	Density	ρ_s	9580	kg/m^3
	Specific Heat (solid)	c_{ps}	146	J/kg-K
	Specific Heat (liquid)	c_{pl}	184	J/kg-K
	Latent heat of fusion	ΔH_f	39800	J/kg
	Melting Temperature	T_m	77.5	ºC
Calculated Properties				
Biot Number Ni		Bi_n	0.000061	-
Biot Number Solder		Bi_s	0.000081	-
Combined Biot Number		Bi_{comb}	0.000174	-
Average Heat Capacity (solid) per m²		Cs_{comb}	1023	J/K-m^2
Average Heat Capacity (liquid) per m²		CL_{comb}	1046	J/K-m^2
Total Mass Solder Layer		m_s	0.608	kg/m^2
Combined Density		ρ_{comb}	8540.0	kg/m^3
Combined Conductivity		k_{comb}	42.0	W/m-K

The first term on the right-hand side, $\left(2\rho_n c_{p,n} t_n + \rho_s c_{p,s} t_s\right)$, can be wrapped into a single heat capacity, C. With the heat loss terms spelled out, and after dividing by A, Eq. (2-3) becomes

$$C\frac{dT_s}{dt} = \alpha\dot{Q}''_{rad} - 2h_c(T_s - T_a) - 2\epsilon\sigma(T_s^4 - T_a^4) \tag{2-4}$$

In Eq. (2-4), $C = \left(2\rho_n c_{p,n} L_1 + \rho_s c_{p,s} L_2\right)$, h_c is the convective heat transfer coefficient, ε is the emissivity of the link's surface, and σ is the Stefan-Boltzmann constant (5.67·10^{-8} W/m^2-K^4). T_s is the link's (surface) temperature and T_a is the temperature of the surroundings. Due to the radiation loss

term in Eq. (2-4), the ordinary differential equation becomes non-linear. Equation (2-4) can be linearized by assuming a radiation-equivalent heat transfer coefficient defined as

$$h_{rad} = \epsilon\sigma \frac{(T_s^4 - T_a^4)}{(T_s - T_a)} \tag{2-5}$$

The assumption of the right-hand side of Eq. (2-5) being constant does not create a large error given the small temperature difference between the link and the surroundings ($T_s \leq T_{act}$). Inserting Eq. (2-5) into Eq. (2-4) gives

$$C\frac{dT_s}{dt} = \alpha\dot{Q}''_{rad} - (2h_h + 2h_{rad})(T_s - T_a) \tag{2-6}$$

Subtracting T_a from the numerator on the left-hand side and rearranging gives a first-order, linear, non-homogeneous differential equation.

$$\frac{d(T_s - T_a)}{dt} + \frac{(2h_h + 2h_{rad})}{C}(T_s - T_a) - \frac{\alpha\dot{Q}''_{rad}}{C} = 0 \tag{2-7}$$

Solving Eq. (2-7) for t when $T_s = T_{act}$ with the initial condition $T_s(t = 0) = T_a$ gives,

$$t_{phase_I} = \frac{C}{(2h_h + h_{rad})}\ln\left[1 - (T_{act} - T_a)\frac{(2h_h + 2h_{rad})}{\alpha\dot{Q}''_{rad}}\right] \tag{2-8}$$

Obviously, a solution for Eq. (2-8) does not exist when the term inside the natural logarithm becomes negative. This makes sense since this would require the heat loss to be greater than the radiant heat in; a situation that would cool the link down rather than heat it up.

The time to heat up the link to its activation temperature is described by Eq. (2-8). The time for the solder to melt depends on the latent heat of fusion ΔH_f of the solder material (e.g., Indalloy 158). Since this would not require a differential equation, the non-linear radiation term can be left in its original form. The time for the solder to melt will then become

$$t_{phase_{II}} = \frac{\rho t \Delta H_f}{\alpha\dot{Q}''_{rad} - (2h_c[T_{act} - T_a] + 2\varepsilon\sigma[T_{act}^4 - T_a^4])} \tag{2-9}$$

The total activation time is the sum of Eqs. (2-8) and (2-9).

$$t_{act} = t_{phase_I} + t_{phase_{II}} \tag{2-10}$$

Equation (2-10) was compared against the IR temperature histories. The linearized assumption for the radiant heat loss term creates very little error compared to the numerical solution. The linearized heat transfer coefficient h_{rad} was found to be 7.1 W/m²-K, which is the average of the value from Eq. (2-5) between T_{amb} and T_{act}. These heat transfer numbers depend on the ambient flow conditions surrounding the sprinkler link, and could differ depending on where the sprinkler is installed.
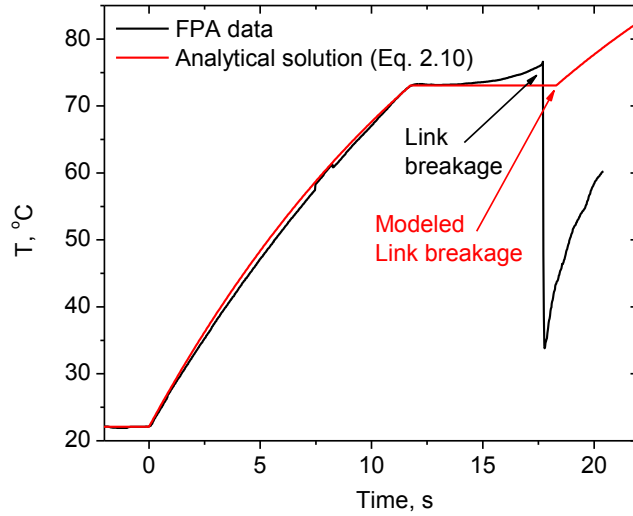
Figure   2-14:   Comparison of calculated and measured link surface temperatures.

Figure 2-14 shows the data from the FPA tested link temperature compared against the calculated temperature. A convective heat transfer coefficient of 24.1 W/m²K was found to best fit the data in this case. The model follows the initial temperature rise very well. At 74°C, the solder starts melting in an isothermal process which is well predicted by the model. After the link breaks the link flies off and the IR camera records the cooler region underneath the link. In the model, once all the solder has melted, the whole system continues to increase in temperature. The predicted sprinkler breakage occurs when all solder has melted, i.e., at the end of the isothermal process. Equation (2-10) allows predicting sprinkler activation based on radiation alone, given all the properties of the fusible link.

3. Evaluation of RAS Using Modified Sprinklers

3.1 Modifications to Convert a Regular Sprinkler into a RAS

The application of the RAS concept was shown by modifying two existing, commercially available sprinkler designs[i]. The conceptual designs were created solely for the purpose of evaluating the RAS concept - future designs are not restricted to the cases tested herein.

Two sprinkler were chosen because they had qualities that made them suitable to be modified into RASs. The two conceptual sprinkler designs are referred to as "RAS A" and "RAS B". Properties and details of these two sprinklers are given in Table 3-1.

RAS A is based on a small, flush, high-sensitivity solder element and lever residential sprinkler. The sprinkler and ceiling ring are available with a 165°F (74°C) temperature rating and come with either a polished-chrome or white-painted finish. The sprinkler is designed for use with concealed piping, mounted flush with the ceiling with the fusible element exposed. The original sprinkler has a fusible element placed outside of the sprinkler body, which makes this design particularly useful when a high view factor with respect to incoming radiation is sought. The thin soldered quick response element allows for short response times.

Table 3-1: Properties and specifications of the sprinklers used in this study[i].

Identifier	RAS A	RAS B
Image		
Position	Pendent	Pendent
Temperature ºC	74	141
Discharge coefficient (K-factor) lpm/bar$^{1/2}$	54	100
Response type	Quick Response (QR)	Fast Response (FR)

---

[i] Product names, brands and other trademarks which may be referenced above are the property of their respective trademark holders. These trademark holders are not affiliated with FM Global and have not sponsored or endorsed this research.

RAS B is based on a residential pendent, recessed, and concealed sprinkler, which is decorative, fast response and uses a frangible bulb element. This sprinkler is designed for use in residential occupancies such as homes, apartments, dormitories, and hotels. The recessed version of the sprinkler is intended for use in areas with finished ceilings. The original sprinkler has a glass bulb element inside a more conventional sprinkler design. The 'Type 30' escutcheon, used to create a flush surface with the ceiling, is attached via three soldered joints.

Both RAS A and RAS B required several modifications to become effective RAS. The modifications made to RAS A will be described first, followed by a detailed description of the modifications made to RAS B.

3.1.1 Modifications to RAS A

Originally, RAS A is available in a chrome and white painted finish. In either case, the sprinkler body and the fusible element itself will be painted white or finished with a shiny chrome layer. Chromium polished surfaces have a low emissivities over the total relevant spectrum of wavelengths with values of $\varepsilon \sim 0.1$ at room temperature and $\varepsilon \sim 0.28\text{-}0.38$ at temperatures in the range 500-1000ºC [6], which makes these surfaces poor absorbers with respect to external radiation. White paint can have high emissivities in the long-wave infrared spectral range. However, the paint type for these sprinklers is not specified. Therefore, the first modification to this sprinkler was to apply a thin layer of thermal absorbent paint (Thurmalox® 270 black stove paint, $\varepsilon \sim 0.96$) onto the fusible element. Elements coated with black high-emissivity paint are shown in Figs. 3-1 and 3-2.

Another modification consisted of applying a small insulating layer on the inside of the fusible element. The insulating material would reduce heat loss through the backside of the element, which is not exposed to any external radiation. The insulating material in this case consisted of one-sided insulating tape. The sprinkler with the fusible element insulated on the backside is shown in Fig. 3-1(a).

Finally, some radiation can be captured and redirected towards the fusible element via a reflector. An example of this is shown in Fig. 3-1(b). For the reflector, some of the original sprinkler housing was used and reversed. No detailed analysis was performed in designing the reflector and more efficient designs can be developed by careful ray tracing of the incoming radiation. The current design, however, serves the purpose of testing the influence of a reflector on the overall sprinkler response. The idea is that some of the radiant energy reflects back onto the fusible element, thus enhancing the heat transfer process. Detailed renderings of the RAS A design are shown in Fig. 3-2.

3.1.2 Modifications to RAS B

Two modifications were made to create RAS B. First, the polished chromium escutcheon plate was coated with high-emissivity thermal paint (Thurmalox® 270 black stove paint, $\varepsilon \sim 0.96$), as shown in Fig. 3-3(a). Second, the glass bulb fusible element was removed and replaced by a stainless steel rod passing through the center of the deflector. An image of RAS B with the escutcheon removed is shown in Fig. 3-3(b). The steel rod or pin presses against the valve and is kept in place by tightening the escutcheon onto the threaded housing. When the solder attached to the escutcheon fuses, the cap flies off, releasing tension of the steel rod and releasing the valve. Since the steel rod might get stuck in place

when not being used for many years, other materials could be used for future designs. Additional 3D views of the final RAS B that was used in the tests are shown in Fig 3-4.

(a)   (b)
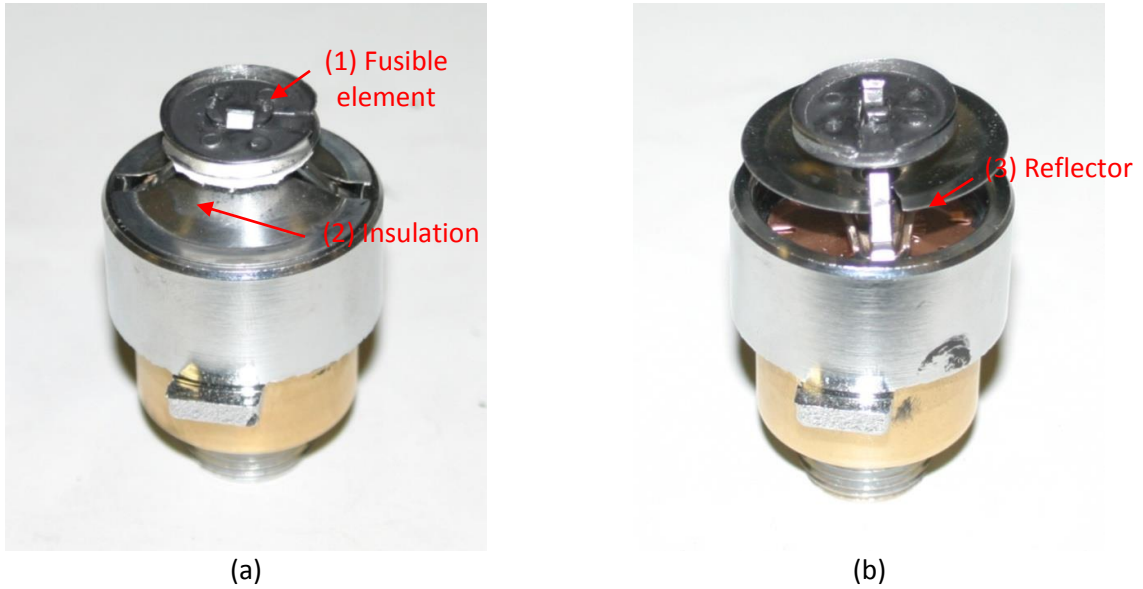
Figure   3-1:   RAS A with high emissivity coating on the fusible element (1) and backside insulated (2) (a). RAS A with high-emissivity coating on the fusible element and a reflector (3) placed behind the fusible element (b)[i (page 18)].

(a)   (b)
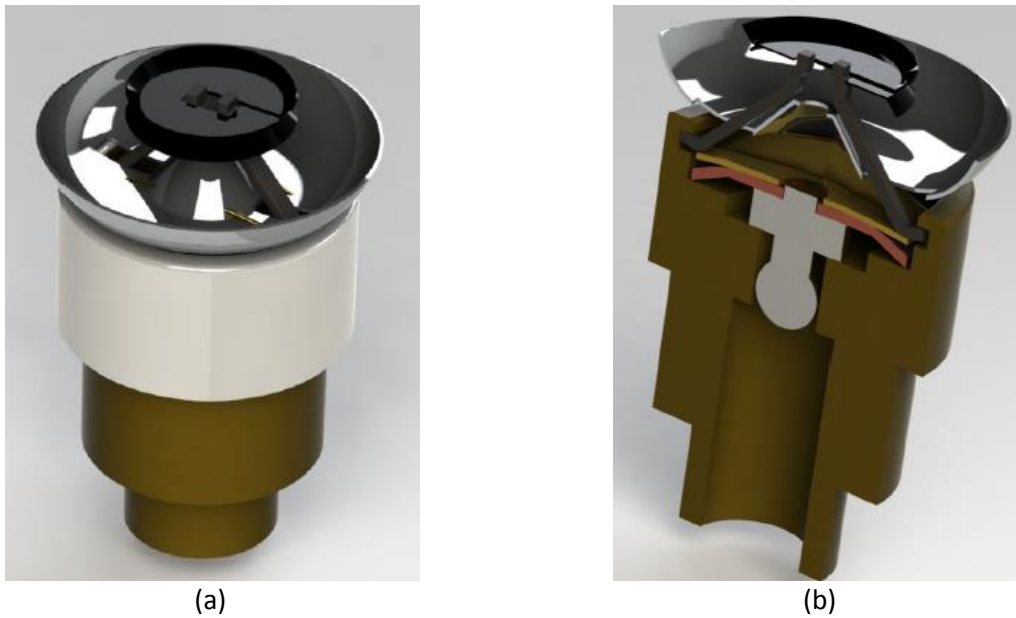
Figure   3-2:   RAS A design view from above (a); cutaway view showing valve assembly (b).

<table>
<tr><td>(a)</td><td>(b)</td></tr>
</table>

(2) Steel pin

Figure   3-3:   RAS B with a high emissivity coating applied to the escutcheon (1) (a). Glass bulb removed and replaced by a solid steel pin (2) (b)[i (page 18)].

(a)   (b)

Figure   3-4:   RAS B design view from above (a); cutaway view showing valve assembly (b).

3.2   Test Design and Modifications

3.2.1 Test Design for RAS A

As described in Section 3.1, the following three major modifications were performed to convert a commercially available sprinkler into RAS A:

- High-emissivity coating applied to the fusible element.
- Insulating the backside of the fusible element
- Placing a reflector behind the fusible element

One would expect that all three modifications benefit the sprinkler's response time when exposed to external radiation. However, the effect of each of these factors has not been quantified. To fully understand the effect each of these three modification, including any potential combined effect, a 2^3

factorial screening test design was used to optimize the response (minimize the sprinkler activation time) and to find the optimum combination of the above listed modifications.

A full factorial test matrix was chosen for this study, resulting in eight individual 'runs' with one repeat. Given the test material and lab time available, a replicate of each test was performed to measure the natural (or common cause) variation in the process. The final experimental matrix is listed in Table 3-2.

Table   3-2:   Full factorial (2^3) experimental design used for testing of RAS A.

Run #	A	B	C	D1	D2	D3	D4	Y1	Y2
	Coating	Insulating Layer	Reflector	Dummy Variables				Response	
1	-	-	-	+	+	+	-		
2	-	-	+	+	-	-	+		
3	-	+	-	-	+	-	+		
4	-	+	+	-	-	+	-		
5	+	-	-	-	-	+	+		
6	+	-	+	-	+	-	-		
7	+	+	-	+	-	-	-		
8	+	+	+	+	+	+	+		

As seen in Table 3-2, all three factors were set at two levels. Factor 'A' represents the application of a high emissivity coating (yes = "+", no = "-"), factor 'B' is the presence of an insulating layer behind the fusible element (yes = "+", no = "-"), and finally, factor 'C' represents the placement of a reflector behind the fusible element (yes = "+", no = "-"). The use of the test matrix shown in Table 3-2 allows for extraction of more information compared to applying the one-factor-at-a-time (OFAT) method. In addition, due to the replication, factors that affect the consistency (variance or experimental error) of the response time of a sprinkler design can be quantified. This is done by calculating the effect of the insignificant dummy variables D1-D4. Dummy variables are variables that, in effect, change nothing.

3.2.2 Test Design for RAS B

For the RAS B prototype, the modifications consisted of applying a high emissivity coating to the escutcheon, removing the glass bulb element and replacing it with a solid steel pin; thus connecting the valve assembly directly to the escutcheon. Since applying a high emissivity coating was the only factor that could change the performance of the sprinkler, no design of experiment approach was used.

3.3 RAS Test Results

3.3.1 RAS A Test Results

The experimental test matrix specified in Table 3-2 does not dictate a heat flux level. Therefore, several tests were run with the unmodified commercially available sprinkler to determine an appropriate heat flux level. Exposing the chromium polished fusible element to 5 kW/m² did not result in sprinkler

activation and the test was aborted after 10 minutes. When the heat flux level was increased to 7.5 kW/m², the uncoated sprinkler activated after a 126 second exposure. Since the uncoated sprinkler was considered to be the slowest prototype; the heat flux level was set to 7.5 kW/m² for all tests, which guaranteed a finite response time for even the "slowest" RAS design. All tests in this matrix were performed at 0º inclination angle (i.e., with the radiation source on the sprinkler axis). The results of the full factorial matrix from Table 3-2 are presented in Table 3-3.

Table   3-3: DOE applied to minimize the response time RAS A.

Run #	A Coat.	B Ins.	C Refl.	D1	D2	D3	D4	Y₁	Y₂	Y_bar	R
1	-1	-1	-1	1	1	1	-1	105	126	115	21
2	-1	-1	1	1	-1	-1	1	46	43	45	3
3	-1	1	-1	-1	1	-1	1	82	115	99	33
4	-1	1	1	-1	-1	1	-1	43	44	44	1
5	1	-1	-1	-1	-1	1	1	26	22	24	4
6	1	-1	1	-1	1	-1	-1	11	16	14	5
7	1	1	-1	1	-1	-1	-1	26	26	26	0
8	1	1	1	1	1	1	1	20	18	19	2
$\sum \bar{Y}_{x_+}$	83	187	121	205	247	202	186				
$\sum \bar{Y}_{x_-}$	302	198	264	180	138	183	199				
Δ	-220	-11	-144	26	109	20	-13				
E_x	-55	-3	-36	6	27	5	-3				
$\sum R_+$	11	36	11	26	61	28	42				
$\sum R_-$	58	33	58	43	8	41	27				
F	27.8	1.2	27.8	2.7	58.1	2.1	2.4				

In Table 3-3, Y₁ and Y₂ are the measured response times in seconds in the two repeat tests performed for the condition. Y_bar is the average of Y₁ and Y₂ and R is the absolute difference between Y₁ and Y₂. Also shown in Table 3-3 are the main effects for each factor, which are calculated using the following equation

$$E_x = \frac{\sum \bar{Y}_{x+} - \sum \bar{Y}_{x-}}{N/2},$$ (3-1)

In Eq. (3-1), E_x is the effect of factor x, $\sum \bar{Y}_{x_+}$, and $\sum \bar{Y}_{x_-}$ are the sum of all average response times with factor x set to "+" and "-", respectively, and N is the total number of runs (2³ = 8 in this case). Since the full factorial design is always orthogonal, the number of "+"and "-" signs is equal for each column [7].

Main effect plots presenting the data from Table 3-3 are shown graphically in Figs. 3-5 and 3-6. Each effect is calculated using Eq. (3-1). The average reduction in activation time due to the high-emissivity coating is 55 seconds. With a reflector placed behind the fusible element, the reduction is 36 seconds. The average effect of insulating the backside of the fusible element is less than 3 seconds.

(a)   (b)
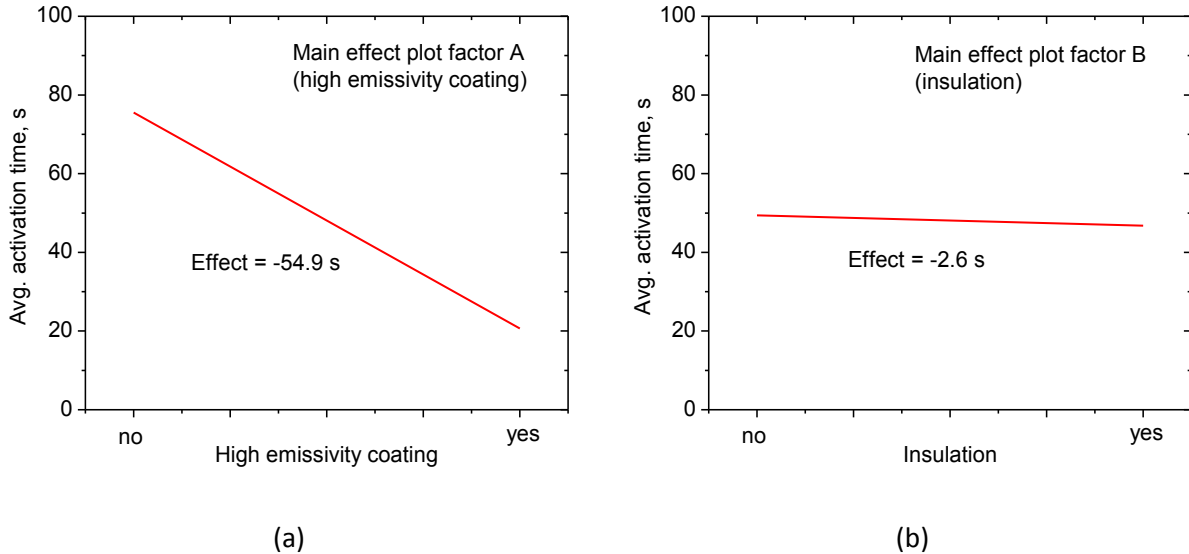
Figure   3-5:   Effect of high-emissivity coating (Factor 'A') on activation time (a). Effect of insulating the backside of the fusible element (Factor 'B') on activation time.

(a)   (b)
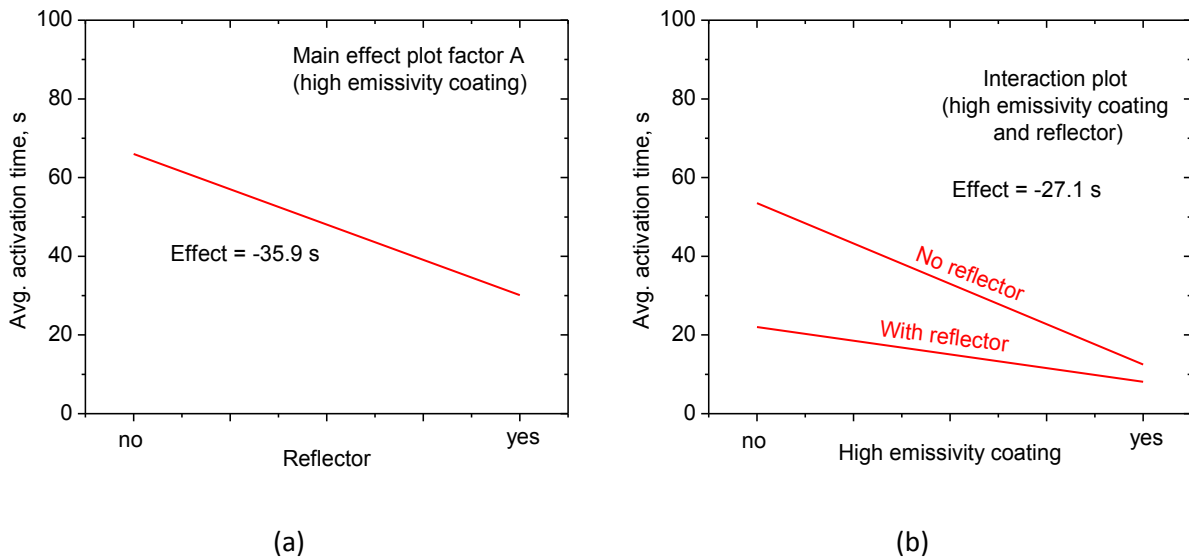
Figure   3-6:   Effect of reflector (Factor 'C') on activation time (a). Effect of the interaction between high-emissivity coating and reflector on activation time (b).

The plots shown in Figs. 3-5 and 3-6, indicate that all three factors (high-emissivity coating, insulation, and reflector) reduce the activation time. Each plot shows one factor without confounding from the other factors due to this factorial experimental design. The significance of each effect can be

determined by differentiating between common causes and special causes of variation, which can be accomplished by establishing control limits (CLs). CLs serve as confidence intervals. As is common in design of experiments (DoE) analysis, the CLs are established at two standard deviations (+ and – 2 σ) around the average. For limited data sets, finding the standard deviation can be problematical; therefore, by convention [7], the standard deviation, σ, was obtained (estimated) using

$$\sigma = \frac{\bar{R}}{d_2} \, ,$$
(3-2)

where $\bar{R} = \sum R/n$. In this case, n = 8. The value for d_2 is selected from a $\bar{x}$ and R chart, which is the control chart used to monitor variable data when samples are collected at regular intervals from a process [7].

A $\bar{x}$ and R chart is particularly useful when the sample size is relatively small. In the case of the data shown in Table 3-3, $\bar{R}$ is 8.63, d_2 is 1.13, and σ is 8.63/1.13 = 7.63. For a two-level factorial design, the variability in any effect is known as the standard error and designated σ_{effect} and is calculated using the following formula:

$$\sigma_{effect} = \sigma\sqrt{4/N},$$
(3-3)

where *N* represents the total number of responses (16 in this case). Therefore,

$$\sigma_{effect} = 7.63\sqrt{4/16} = 3.81 \, .$$
(3-4)

Given the limited size of our sample, there is not much 'freedom' to accept σ_{effect} as the accurate estimate of the standard error. The CLs are calculated by multiplying σ_{effect} by the student's t-value based on the available degrees of freedom (df), which is calculated in general for *p* factors (3) and *n* replicates (1) as follows:

$$df = 2^p(n-1) \, .$$
(3-5)

Given the degrees of freedom, the student's *t*-distribution at 95% confidence level can be determined via standardized statistical tables [7] The CLs are

$$CL = + \text{ and} - t(\sigma_{effect}) \, ,$$
(3-6)

$$CL = + \text{ and} - 2.31(3.81) \, ,$$
(3-7)

$$CL = + \text{ and} - 8.80 \, .$$
(3-8)

The CLs calculated above determine that any effect greater than 8.8 seconds can be deemed significant. Therefore, given the calculated effects shown in Figs. 3-5 and 3-6, the effect of high-emissivity coating and the use of a reflector reduce the activation times significantly. Insulation of the backside of the fusible element does not reduce the activation time significantly, because the backside of the fusible

element does not lose a significant amount of heat. The interaction between the high-emissivity coating and the reflector appears to create a significant effect. This interaction is also shown in Fig. 3-6(b), where the effect of the reflector is much more profound when the fusible element is left uncoated.

Understandably, when a high-emissivity coating is applied to the front surface of the fusible element, a significant amount of heat is captured through the front side of the element and the heat redirected by the reflector is less important. Given the fact that a reflector significantly reduces the sprinkler activation time when exposed to external radiation, a quick experimental validation was performed into the effect of applying a high-emissivity coating to the backside of the fusible element as well. A backside coating could theoretically improve the absorbance of any reflected radiation. Two tests with backside coating were performed at the same conditions (7.5 kW/m^2) as all the data collected and shown in Table 3-3. The result of this is shown in Table 3-4. All four tests shown in Table 3-4 were performed with the front of the fusible element coated and a reflector in place. Run 2 had the backside of the reflector coated as well. The data shown for Run 1 in Table 3-4 are taken from Table 3-3 (Run 6) and show the results with the backside uncoated. The data listed in Table 3-4 show that applying a high emissivity coating to the backside of the fusible element does not affect the response time significantly.

Table   3-4:   Test results investigating the effect of backside coating.

Run #	Backside of fusible element coated (yes/no)	Y_1	Y_2	Y_{bar}	S
1	no	11.0	16.0	13.5	3.5
2	yes	16.0	14.0	15.0	1.4

With the reflector present, insulation on the backside of the fusible element tends to increase the response time. Backside insulation increases the response time by blocking reflected radiation. This hypothesis can be tested based on the data in Table 3-3 alone, which are rearranged and shown in Table 3-5. Even with limited data, applying backside insulation does increase the activation time when a mirror is present.

Table   3-5:   Test results investigating the effect of backside insulation.

Run #	Backside insulation	Y_1	Y_2	Y_{bar}	S
1	yes	20.0	18.0	19.0	1.4
2	no	11.0	16.0	13.5	3.5

Given the results and analysis thus far, the <u>ideal</u> RAS prototype is one which has the front side of the fusible element coated with high-emissivity paint and a reflector placed behind the fusible element.

To further understand the response of RAS A to various levels of external radiation, this prototype sprinkler was tested at radiation levels ranging from 2.0 kW/m^2 to 7.5 kW/m^2. The effect of the inclination angles with respect to radiant source was also tested. This was done by measuring the difference in operating time between RAS exposed at 0° and 45°. The results are shown in Fig. 3-7. Sprinkler activation due to external radiation was accomplished at radiation levels as low as 3.0 kW/m^2. However, with the radiation source aligned at 45° from the axis of the sprinkler, 3.0 kW/m^2 resulted in an operating time close to 9 minutes, which may not be acceptable. In the RAS design phase, the sprinkler sensitivity can be manipulated. Based on the results of the DoE analysis on the RAS A prototype, sensitivity to the incoming radiation can be controlled by either removing the reflector or by using a coating on the fusible element with a lower known emissivity. Using a higher temperature rated fusible element could also be an option if lower sensitivity to external radiation is desired.

In summary, the RAS A design is very effective, potentially operating at heat flux levels of 3.0 kW/m^2 and above.
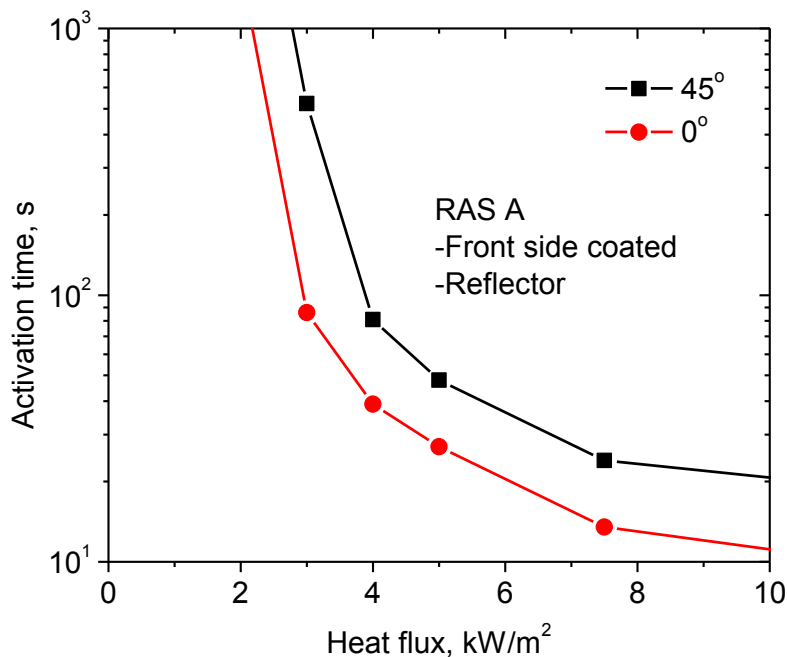
Figure   3-7:   Activation time versus external heat flux for the RAS A prototypes. Data collected with the radiant source at 0° and 45° inclination angle from the sprinkler axis.

3.3.2 RAS B Test Results

RAS B was described in Section 3.1. The idea behind this design was to utilize the release mechanism of the escutcheon normally used for concealing the sprinkler. The release mechanism consists of three soldered 57 °C attachment points and a spring loaded release mechanism. The modification made in this

study was to remove the glass bulb fusible element and replace it with a solid steel pin, which holds the valve in place. Once the solder attachment points melt, tension on the steel pin is removed releasing the valve assembly.

In addition to replacing the glass bulb fusible element, the original chromium escutcheon was coated with a high emissivity paint to improve the emissivity (see Figs. 3-3 and 3-4). All test results are shown in Table 3-6. The effect of applying a high-emissivity coating to the escutcheon was tested at heat flux levels ranging from 3 kW/m² to 9 kW/m². Coated sprinklers were tested at 0° and 45° inclination angle.

Table   3-6:   Test results of the RAS B prototype.

Distance	Heat Flux	Time (coated) 0º		Time (coated) 45°	Time (not coated) 0º
cm	kW/m²	s	s	s	s
113	8.15	17	16	33	167
135	6.1	28	24	64	no activation
150	5.0	36	34	94	no activation
168	4.0	52	59	88	no activation
193	3.0	110	135	234	no activation

For external radiation levels below 7.5 kW/m², the escutcheon should be coated with high-emissivity paint for the sprinkler to activate. For each "no activation" entry in Table 3-6, the sprinkler was exposed for 10 minutes before the test was terminated. Each coated sprinkler was exposed to external radiation at 0° and 45° angles. Table 3-6 shows highly repeatable results with heat fluxes as low as 3 kW/m². The data in Table 3-6 are shown graphically in Fig 3-8.

Increasing the inclination angle of the fusible element with respect to the incoming radiation from 0° to 45° increased the operating time, on average, by a factor of 2.3.

3.4   Thermal Analysis

With conventional convectively-activated sprinklers, radiation is not given much consideration. The convective heat transfer rate, $\dot{q}''_{conv}$, to the fusible element is described by Newton's law of cooling (heating), which states that the rate of heat loss of a body is proportional to the difference in temperatures between the body and its surroundings and is described by

$$\dot{q}''_{conv} = hA(T_g - T_d)$$

(3-9)
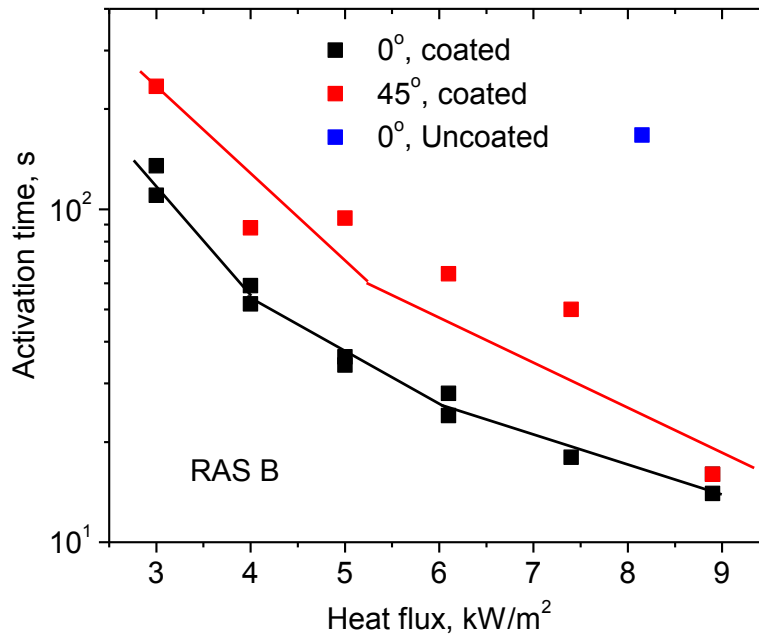
Figure 3-8: Activation time versus external heat flux for RAS B. Data collected at 0° and 45° inclination angle with respect to the radiant source. Uncoated samples are represented by the blue squares.

where h is the convective heat transfer coefficient in kW/m²-K, A is the area being heated in m², T_g is the gas temperature in °C, and T_d is the temperature of the fusible element in °C. In general, the element can be assumed to be thermally thin and temperature gradients within the element are negligible. The element can therefore be treated as a lumped mass. The change in temperature of this mass is given by

$$\frac{dT_d}{dt} = \frac{hA(T_g - T_d)}{mc} \tag{3-10}$$

Were c is the specific heat of the element being heated in J/kg-K. Typically, a time constant can describe the convective heating of a sprinkler fusible element,

$$\tau = \frac{mc}{hA}. \tag{3-11}$$

For many cases, the heat transfer coefficient, h, is roughly proportional to the square root of the Reynolds number ($Re = \frac{ud}{v}$) where u is the gas velocity in m/s, d is the diameter of a cylinder or sphere exposed to convective heating in m, and v is the kinematic viscosity of the gas in m²/s [8]. The fact that h (and therefore τ) is approximately proportional to the square root of the velocity of the gases passing by, results in an expression for the Response Time Index (RTI), which, for a given detector can be expressed as

$$RTI = \tau u^{\frac{1}{2}}.$$

(3-12)

The sprinkler's RTI can subsequently be measured in the laboratory using a plunge-tunnel test. Since the RTI is used to characterize response of conventional sprinklers, one would be interested in finding a similar parameter that can describe a RAS.

For a RAS the only aspect that changes is the heat transfer mode the sprinkler relies on for operation. When a RAS is exposed to external radiation, there may still be a convective component present. When the radiant source is at a sufficient distance from the fusible element, the temperature of the gases surrounding it may be low and the convective component will act as a cooling effect, counteracting the heating due to radiation. The heat transfer equation of a RAS can be described as.

$$mc\frac{dT_d}{dt} = A\alpha\dot{q}''_{rad} + 2Ah(T_g - T_d)$$

(3-13)

where m is the fusible element's lumped mass in kg, c is the specific heat of the element J/kg-K, A is the area of the element on each side m², α is the absorptivity of the element's surface, and $\dot{q}''_{rad}$ is the radiant heat flux in kW/m². The convective heat loss occurs on either side of the fusible element; hence the total surface area of 2A is included in Eq. (3-13). Equation (3-13) is a first order ordinary differential equation (ODE) whose solution is

$$T_d = T_g + \frac{\alpha\dot{q}''_{rad}}{2h}\left(1 - e^{-t/\tau}\right)$$

(3-14)

where the time constant τ is defined as

$$\tau = \frac{mc}{2hA}$$

(3-15)

Setting T_d in Eq. (3-14) to T_f (the fusing temperature of the element) and solving for t result in

$$t = -\tau \ln\left[1 - (T_g - T_f)\frac{2h}{\alpha\dot{q}''_{rad}}\right]$$

(3-16)

The values for τ and h were found for the data obtained with the RAS A sprinkler design by using a generic optimization algorithm. Figure 3-9 shows the results graphically. Data collected at 45° inclination angle with respect to the radiant source (RAS A - based models only) were corrected by dividing the heat flux for these data points by $\sqrt{2}$. With h set to 26.5 *W/m²-K* for either case, the time constant, τ, was found to be 32.4 s and 47.0 s for the RAS A and RAS B model, respectively. The value for h appears high for a case with only natural convection. This might be due to some motion of the air inside the Small Burn Lab. In general, the form given by Eq. (3-16) agrees reasonably well with the data obtained. This result shows that a time constant can be assigned to RAS, which can be used for comparing different RAS against each other. It should be pointed out that the convection coefficient found during the optimization should also be recorded, since the time constant might differ at different values of h [cf. Eq. (3-15)]. In this study the time constant analysis showed that the RAS A based model is slightly more sensitive and reacts faster than the RAS B model.
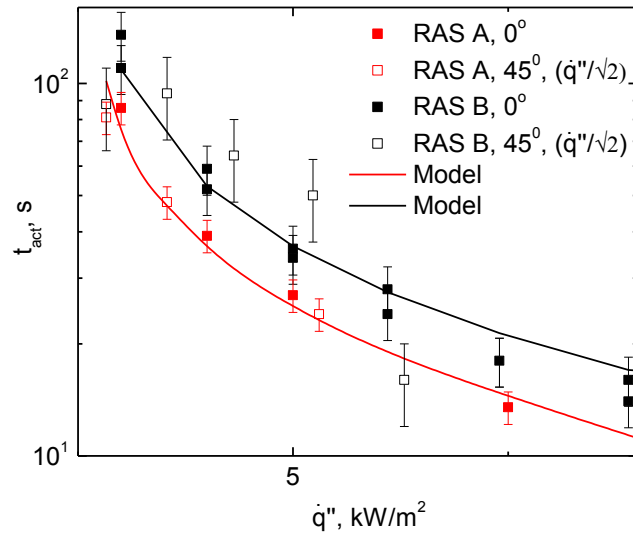
Figure 3-9: Activation time versus external heat flux for the RAS A and RAS B prototypes, solid lines represent results from Eq. (3-16)

4.   Demonstration of RAS Effectiveness in Fire Tests

This section seeks to demonstrate the effectiveness of RAS when compared to a conventional commercially available sprinkler in the absence of a hot ceiling layer. This was accomplished by exposing either RAS A or RAS B to a pool fire, side-by-side with a commercially available conventional QR sprinkler.

4.1   Test Setup

Figure 4-1 shows a picture of the test setup. A 1.0-m diameter heptane pan fire was placed centered under the North movable ceiling inside the LBL. A single 5.1-cm diameter pipe was placed 3.0 m above the surface of the heptane pool. A RAS (Either RAS A or RAS B) and a conventional QR sprinkler were placed on either side of the pool, at a 2.0 m horizontal distance from the pool's centerline (shown by the dashed vertical line in Fig. 4-1). The pressure inside the pipe was monitored using an electronic pressure transducer (Setra, 0-10 bar).

Close-up pictures of the tested sprinklers are shown in Fig. 4-2(a)-(c). Figure 4-2 (a) shows the conventional QR pendent sprinkler, Fig. 4-2(b) shows the installed RAS A, and Fig. 4-2(c) shows the installed RAS B. Figure 4-3(a) and (b) show the RAS A and RAS B sprinkler, respectively, installed on the pipe and photographed from below.
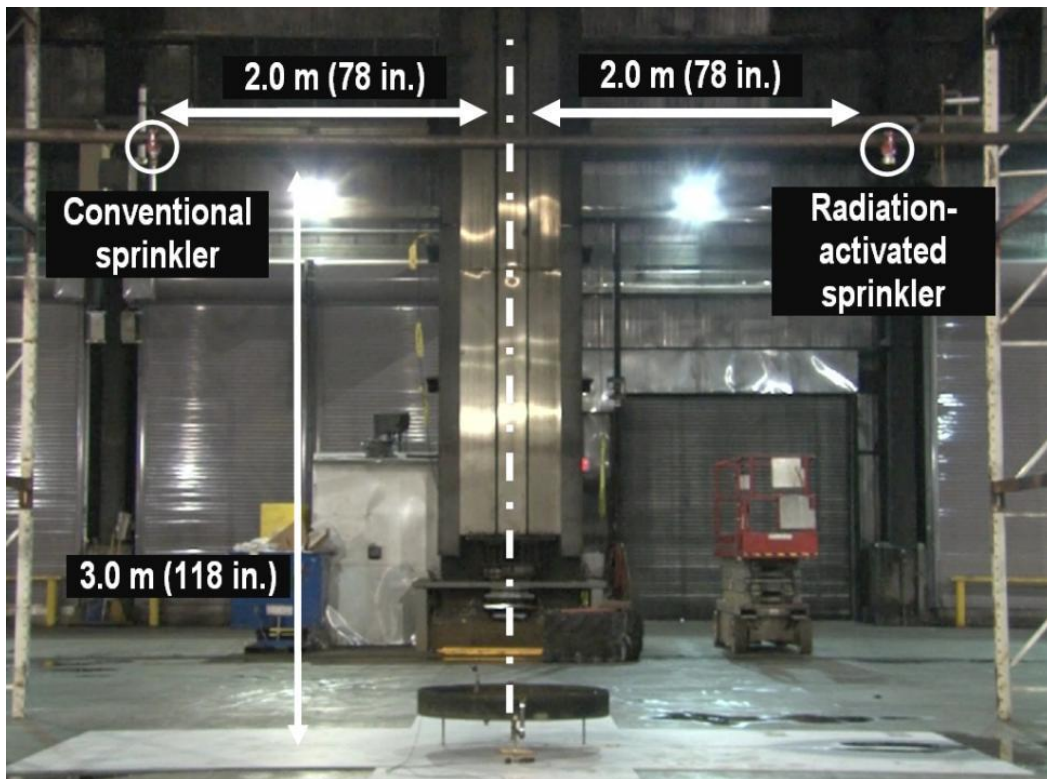
Figure   4-1:   Picture of the test setup used for the side-by-side tests.

(a)   (b)   (c)
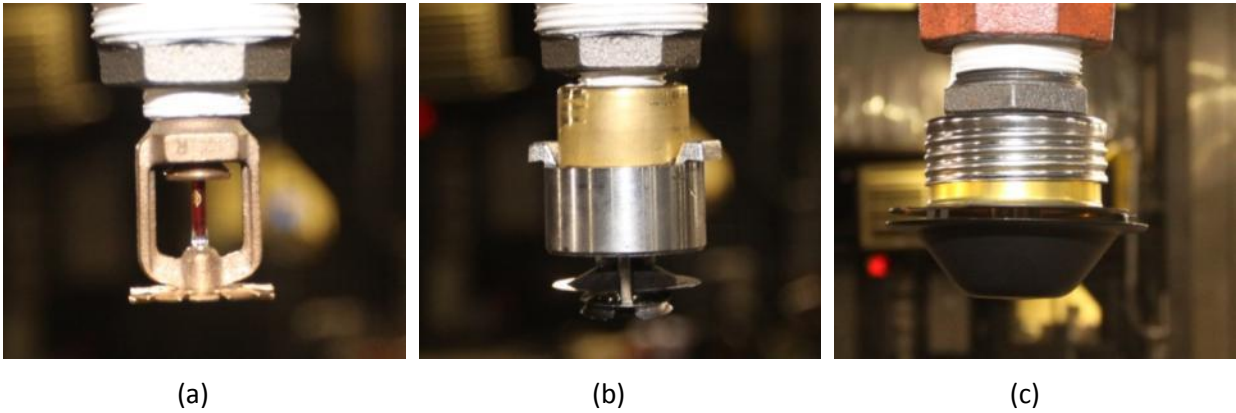
Figure   4-2:   Images of tested sprinklers: (a) conventional QR sprinkler; (b) RAS A; (c) RAS B[ii].

(a)   (b)
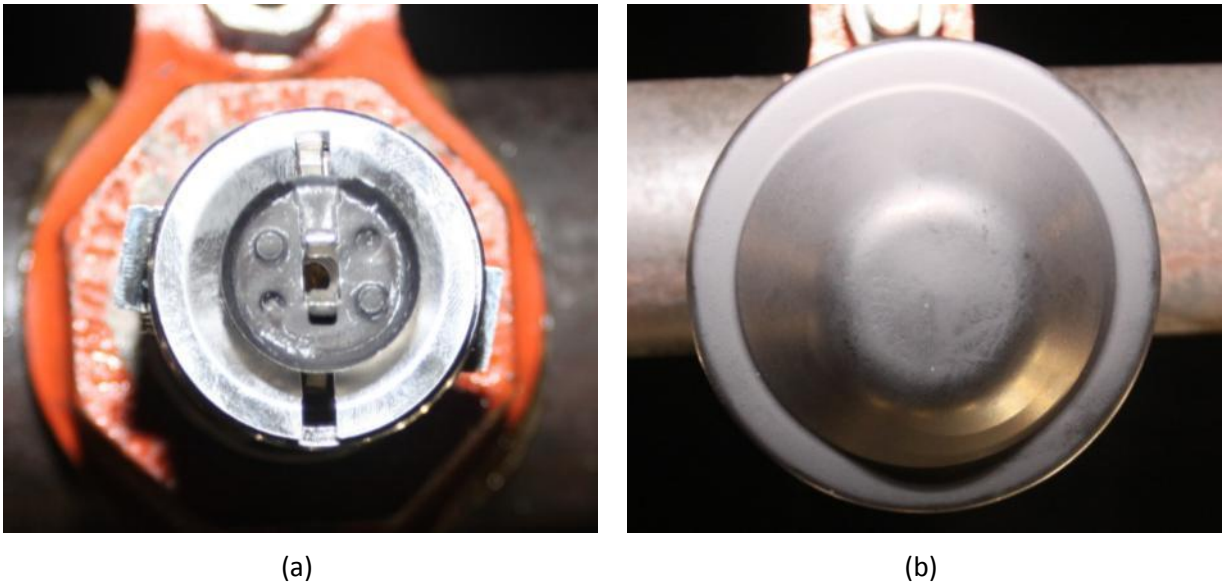
Figure   4-3:   Images taken from below of the installed RAS A (a) and RAS B (b)[i (page 18)].

The experimental procedure started with installing two new sprinklers (both conventional and RAS) on the pipe. The conventional sprinkler, although not activated in a previous test, was replaced by a new one to ensure the fusible element heated above ambient from a prior test was not used.

The fire exposure consisted of a circular pan (1-meter in diameter) filled with a layer of heptane (1.2 cm in thickness). The pan was ignited using a propane torch. Each test resulted in a burning duration of approximately 5 minutes. The test was terminated after all the fuel was consumed. Sprinkler activation times were determined from the recorded video footage and were defined as the time between ignition and the activation of the sprinkler.

4.2 Experimental Results

Ten pool fire tests were conducted. Figure 4-4 shows a screenshot taken one minute after igniting the heptane pan fire. Appendix B shows video frames taken at regular time intervals during each of the ten tests.

Figure   4-4:   Screenshot taken during Test 1.

Experimental results from the ten side-by-side tests are summarized in Table. 4-1, where activation times are listed in seconds. The average heat flux shown are estimated by solving Eq. (3-16) for $\dot{q}''$ given the measured activation time. Pressures inside the branch pipe were measured and recorded. The average heat flux resulting from all sprinkler tests was 2.8 ± 0.39 kW/m^2. While these heat fluxes were not directly measured, they provide a reasonable estimation of the radiant heat flux reaching the RASs.

For RAS A, activation times varied between 64 and 126 seconds. The location of the sprinkler was switched between the North and Sound side of the sprinkler branch pipe to average out any flame leaning effects due to drafts in the lab. In general, flames leaned slightly toward the South, resulting in faster activation when the sprinkler was installed on that side.

Five tests were carried out using RAS B. During the first test, some suppression water got trapped inside the dome-shaped escutcheon. Presumably, this happened because of an imperfect seal around the plug. Due to the water cooling the dome shape element, this test never resulted in sprinkler operation. To avoid water being trapped inside the dome, for the remaining tests sprinklers were installed on a dry pipe, and a valve was opened manually after sprinkler activation was observed.

The conventional QR pendent sprinkler failed to operate in all but one occasion (Test 3). During this test, water sprays from the activated RAS A pushed the flames towards the conventional sprinkler (see Fig 4-5), leading to its activation.

Table 4-1: Activation times and calculated heat fluxes at the fusible link using Eq. (3-16).

Test #	Sprinkler Type	Position	t_{act} (s)	$q''_{derived}$ (kW/m^2)
09-Sep-14, T_{inside} 21ºC (70ºF), RH_{inside} 60%, $T_{outside}$ 19ºC (67ºF), $RH_{outside}$ 61%				
1	RAS B		no activation	
2	RAS A	North	124	2.3
3	RAS A		126	2.3
4	RAS A	South	68	3.1
5	RAS A	North	92	2.7
6	RAS A	South	64	3.2
10-Sep-14, T_{inside} 20ºC (68ºF), RH_{inside} 68%, $T_{outside}$ 17ºC (62ºF), $RH_{outside}$ 79%				
7	RAS B		81	3.4
8	RAS B	North	106	3.0
9	RAS B		139	2.6
10	RAS B		120	2.8

Figure 4-5: Flame leaning caused by activated RAS sprinkler on the right resulting in the activation of the conventional sprinkler.

4.3 Consistency between Side-by-side Test Results and Individual Sprinkler Tests

This section shows how a multi-node source method can assist in predicting the radiant heat flux for a given fire. The predictions made using this analysis should show that the sprinkler response times measured in the side-by-side test are consistent with estimates response time of the sprinklers based on the calculated radiant heat flux from the pool fire using the multi-node source method.

During the side-by-side tests, the fire size could be estimated using the correlation provided by Ditch et al. [9] which for a 1-m diameter pool fire results in a burning rate of approximately 57 g/m^2-s. For the 0.785 m^2 pool used in this study, the total mass burning rate becomes 44.6 g/s. Given a theoretical heat of combustion, ΔH_c, of 44.78 kJ/g, the total fire size then becomes 2.0 MW. The average flame height can be calculated using the following correlation developed by Heskestad [10].

$$L_f = -1.02D + 15.6 \left[\frac{c_p T_\infty \dot{Q}^2}{g \rho_\infty \left(\frac{\Delta H_c}{r} \right)^3} \right]^{1/5}$$

(4-1)

Equation (4-1) gives the mean luminous height of a buoyant turbulent diffusion flame. In Eq. (4-1), L_f is the flame height in meters, D is the pool diameter in meters, c_p is the specific heat of air (~1.008 kJ/g-K), T_∞ is the ambient air temperature in K, $\dot{Q}$ is the theoretical heat release rate (kW), g is the gravitational constant (m/s^2), ρ_∞ is the ambient air density (~1.2 kg/m^3), ΔH_c is the theoretical heat of combustion (kJ/g), and r is the stoichiometric air-to-fuel mass ratio (15.1 for heptane). Given a 1-m diameter pool fire at a theoretical heat release rate of 2.0 MW, the flame height, L_f, based on Eq. (4-1) was calculated to be 4.1 m. This flame height agrees well with observations shown in Appendix A.

With the fire size characterized for this study ($\dot{Q} = 2.0\ MW, L_f = 4.1\ m$), the expected heat flux at the thermal link can be estimated using a multi-node source method. This method for estimating radiant heat fluxes is described in greater detail by Hankinson and Lowesmith [11]. The method consists of dividing the fire plume in multiple nodal sources. Each point source is given a weight, w_i, which follows a specified distribution. A graphical representation of this method is presented in Fig. 4-6.

The following assumptions are made when using the multi-node source method:

- The time-averaged flame shows an approximately conical profile.
- The main mode of heat transfer is radiation to the fusible link.
- The flame stays symmetric around the center axis of the conical profile (no tilting/leaning).
- The maximum radiation comes from the node located at the flame centroid, *i.e.*, (0.25L_f).
- Flame transmissivity is 1, i.e., under the optically thin condition.
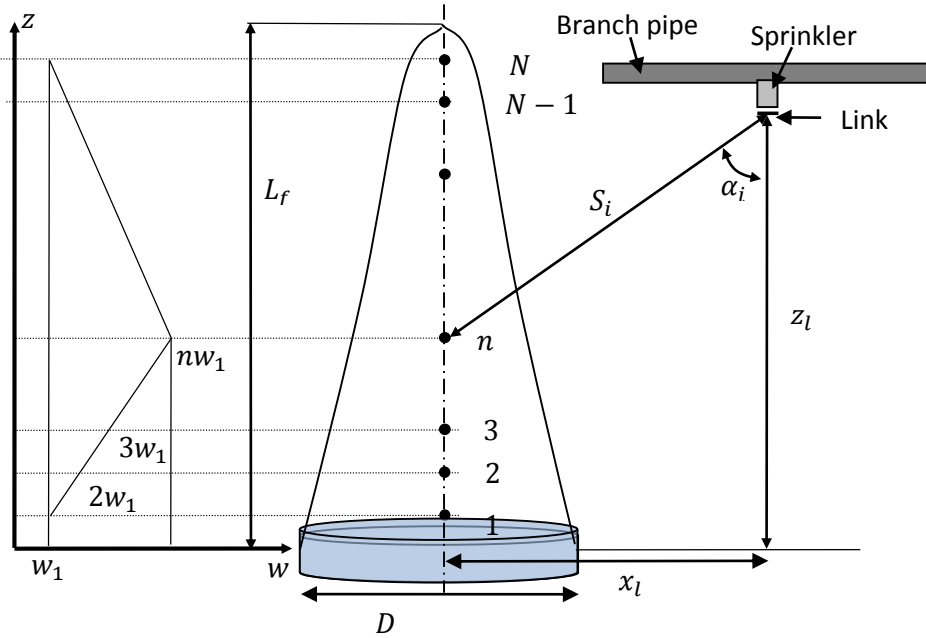
Figure   4-6:   Geometry setup for the weighted multi-node radiation source method.

While the above criteria may not be all fully applicable, the overall result using the multi-node method has been shown to be more accurate compared to using the singe point source method [11]. In the multi-node source method, heat fluxes at a single location are assumed to be received from N point sources distributed along the flame's vertical axis. The received radiation is determined as the weighted sum of the radiation from each individual point source as given by the following equation:

$$\dot{q}_l'' = \sum_{i=1}^{N} w_i \frac{\chi_r \dot{Q} \tau_i}{4\pi S_i^2} cos\alpha_i$$

(4-2)

In Eq. (4-2), $\dot{q}_l''$ is the heat flux received by the fusible link, χ_r is radiant fraction of heptane, w_i is the weighing factor of the ith point, $\dot{Q}$ is the total chemical heat release rate, S_i is the distance of the ith node to the fusible link, τ_i is the transmissivity over distance S_i, and α_i is the angle between S_i and the normal direction of the link surface. N is the number of nodes selected for the analysis. In this study the radiant fraction, χ_r, was set to 0.32.

Taking τ_i to be 1 for all point sources is a good approximation for the present experiments as no considerable atmospheric radiation absorption (due to CO_2 and water vapor) is expected in the short distance between the sprinkler link and the flame.

The individual weight, w_i, assigned to each node was determined as follows:

$$w_i = \begin{cases} iw_1 & \rightarrow 1 \le i \le n \\ \left[\dfrac{(i-N)(1-N)}{N-n} + 1 \right] w_1 & \rightarrow n+1 \le i < N \end{cases}$$

(4-3)

where the sum of all weight factors equals one so that

$$\sum_{i=1}^{N} w_i \equiv 1 \qquad (4\text{-}4)$$

Equation (4-3) is shown schematically on the left side in Fig. 4-6 with weights increasing linearly to a peak at the nth point (where $w_n = nw_1$) and decreasing linearly thereafter so that $w_N = w_1$. After some algebraic derivation, it follows from Eqs. (4-3) and (4-4) that the "base" weight, w_1, can be given by the following equation:

$$w_1 = \frac{2}{(1+n)N+(1-n)} \cdot \qquad (4\text{-}5)$$

S_i in Eq. (4-2) can be calculated through geometric means as

$$S_i = \sqrt{x_l^2 + [(i-1/2)\Delta z - z_l]^2} \qquad (4\text{-}6)$$

In Eq. (4-6), x_l is the horizontal distance between the link and the center of the pan in meters, $\Delta z = L_f/N$, and z_l is the vertical distance between the link and the liquid surface in meters. z_l and x_l were fixed at a distance of 3.0 m and 2.0 m, respectively.

Finally, the incident angle, α_i, of the incoming radiation with respect to the outward drawn normal of the heat responsive element changes for each nodal source calculation. The angle, α_i, is taken with respect to the axis of the sprinkler's orifice. Any radiant heat flux coming from the portion of the flame above the sprinkler location (i.e., $\alpha_i > 90°$) does not participate in heating the element, so that:

$$\alpha_i = \begin{cases} \sin^{-1}(x_l/S_i) & \rightarrow (i-1/2)\Delta z \le z_l \\ \pi/2 & \rightarrow (i-1/2)\Delta z > z_l \end{cases} \qquad (4\text{-}7)$$

The predicted radiant heat flux at the heat responsive element using both multi-node and single node methods is summarized in Table 4-2. With N set to 40 and n set to 10 (i.e., the peak weight located ¼ of the flame height above the pool), the predicted heat flux at the thermal link was calculated to be 3.5 kW/m². This value decreases to 3.3 kW/m² when the peak weight is shifted to one half the flame height (i.e., n = 20). Giving each w_i equal weight of $w_i = w_1 = 1/N$ results in a heat flux of 2.7 kW/m².

The values found using the multi-node analysis are significantly lower compared to using the single point source method. Table 4-2 shows that heat fluxes ranging from 4.5 kW/m² to 4.8 kW/m² are estimated when a single node is used at 25% and 33% of the flame height, respectively.

When the calculated heat fluxes are compared to the derived values based on the experimental results listed in Table 4-2, the multi-node heat flux predictions show reasonable agreement with the heat fluxes derived from the sprinkler's measured activation times. Using a weighted scheme, Eq. (4-2), does not show much difference over equally dividing each weight over each of the 40 nodes. Using the latter

method results in a predicted heat flux of 2.7 kW/m², which agrees well with derived averaged heat flux of 2.8 kW/m², again based on the observed activation times.

Table 4-2: Predicted radiant heat flux at the fusible link using multi-node and single node methods.

Method	w_i	n	N	$\dot{q}_l''$ kW/m²
Multi-node	Eq. (4-3)	10	40	3.5
	Eq. (4-3)	20	40	3.3
	1/N	N/A	40	2.7
Location of single node as a % of L_f				$\dot{q}_l''$
Single Node	25% (103 cm above the pool)			4.5
	33% (138 cm above the pool)			4.8
	50% (208 cm above the pool)			4.4

The above analysis demonstrated that the multi-node analysis can provide reasonably accurate results with respect to providing guidance to calculate radiant heat fluxes reaching a heat responsive element from a known fire source. Ideally, future model validation will be based on direct heat flux measurements. Understanding how to estimate the expected heat flux levels can help determine the installation guidance on the newly designed RASs.

5. **Summary and Conclusions**

Conventional sprinklers operate due to convective flow of hot gases passing the heat responsive element, which render them ineffective in situations where hot ceiling layers are not formed. In this study, a new conceptual sprinkler design, defined as radiation-activated sprinkler (RAS), is proposed that can activate when exposed to external radiation.

The benefit of the RAS as a protection solution includes limiting the exposure from hazards such as external exposure protection, sprinkler protection beneath grated mezzanines, and special fire hazards such as covered open yard storage. This study has been structured in three phases.

In the first phase, individual fusible elements, removed from their sprinkler housing, were tested using the Fire Propagation Apparatus (FPA) at heat fluxes ranging between 2 and 10 kW/m^2.

The second phase focused on the development and testing of the application of the RAS. Two RASs were designed, fabricated, and tested. This second phase successfully demonstrated the development of a RAS by applying practical modifications to existing sprinkler types. These adapted sprinkler designs have great potential in protecting situations were conventional sprinklers are ineffective.

The effect of modifications on the first RAS (labeled RAS A) was studied systematically using a Design of Experiments (DoE) approach. For the second RAS (referred to as RAS B) design, only the effect of a high emissivity coating was investigated.

The testing of both RAS A and B led to the following conclusions:

- When exposed to external radiation, the RAS developed in this study were capable of operating at heat flux level as low as 3.0 kW/m^2.
- For the prototypes tested, the greatest effect with respect to increasing the sensitivity of the RAS is accomplished by applying a high-emissivity coating to the fusible element.
- For the prototypes tested, the second greatest effect is accomplished by placing a reflector behind the fusible element – this redirects some of the incoming radiation back onto the fusible element.
- The effect of both backside insulation of the fusible element or a high emissivity coating applied to the backside of the element is statistically insignificant.

In the third and final phase, the effectiveness of applying the RAS concept was demonstrated using a heptane pool fire scenario. The results of ten tests showed that the two developed RAS types activated after a 60-140 second exposure to the pool fire. Conventional, quick response (QR), pendent glass-bulb sprinklers placed at equal distance from the pool fire failed to operate in all but one test, clearly demonstrating the effectiveness and benefits of RAS.

Using multi-node source analysis resulted in predicted radiant heat fluxes that reasonably agreed with those inferred from the measured activation times. The multi-node analysis can be used to estimate RAS

activation times when reasonable estimates of the fire exposure can be made and hence support specific installation design guidance.

References

1. B.D. Ditch, "The Fire Hazard of an Ethanol Process Facility," *Process Safety Progress* , vol. 30, no. 4, pp. 365 - 371 , December 2011.

2. FM Global, "Installation Guidlines for Automatic Sprinklers," in *Loss Prevention Data Sheets 2.0.*, January 2014.

3. ASTM E 2058, "Standard Test Methods for Measurement of Synthetic Polymer Material Flammability Using a Fire Propagation Apparatus (FPA)," ASTM, Conshobocken, PA, Standard 2009.

4. ISO 12136, "Reaction to Fire tests – Measurement of Material Properties Using a Fire Propagation Apparatus," International Organization for Standardization, Geneva, Switzerland, Standard 12136, 2011.

5. FLIR. (2011) www.flir.com/US.

6. M.A. Bramson, *Infrared Applications, A Handbook for Applications*. NY: Plenum Press, 1968.

7. J.F. Leonard, *Design of Experiment*.: WPI Corporate and Professional Workshop, 2000.

8. J.O. Hollman, *Heat Transfer*. New York: McGraw-Hill, 1976.

9. B.D. Ditch, J.L. de Ris, T.K. Blanchat, M. Chaos, R.G. Bill, and S.B. Dorofeev, "Pool Fires - an Empirical Correlation," *Combustion and Flame*, vol. 160, no. 12, 2013.

10. G. Heskestad, "Luminous Height of Turbulent Diffusion Flames," *Fire Safety Journal*, vol. 5, pp. 103-108, 1983.

11. G. Hankinson and B.J. Lowesmith, "A Consideration of Methods of Determining the Radiative Characteristics of Jet Fires," *Combustion and Flame*, vol. 159, pp. 1165-1177, 2012.

Appendix A.   Selected Video Frames

0	30
1:00	1:30
2:00	2:30
3:00	3:30
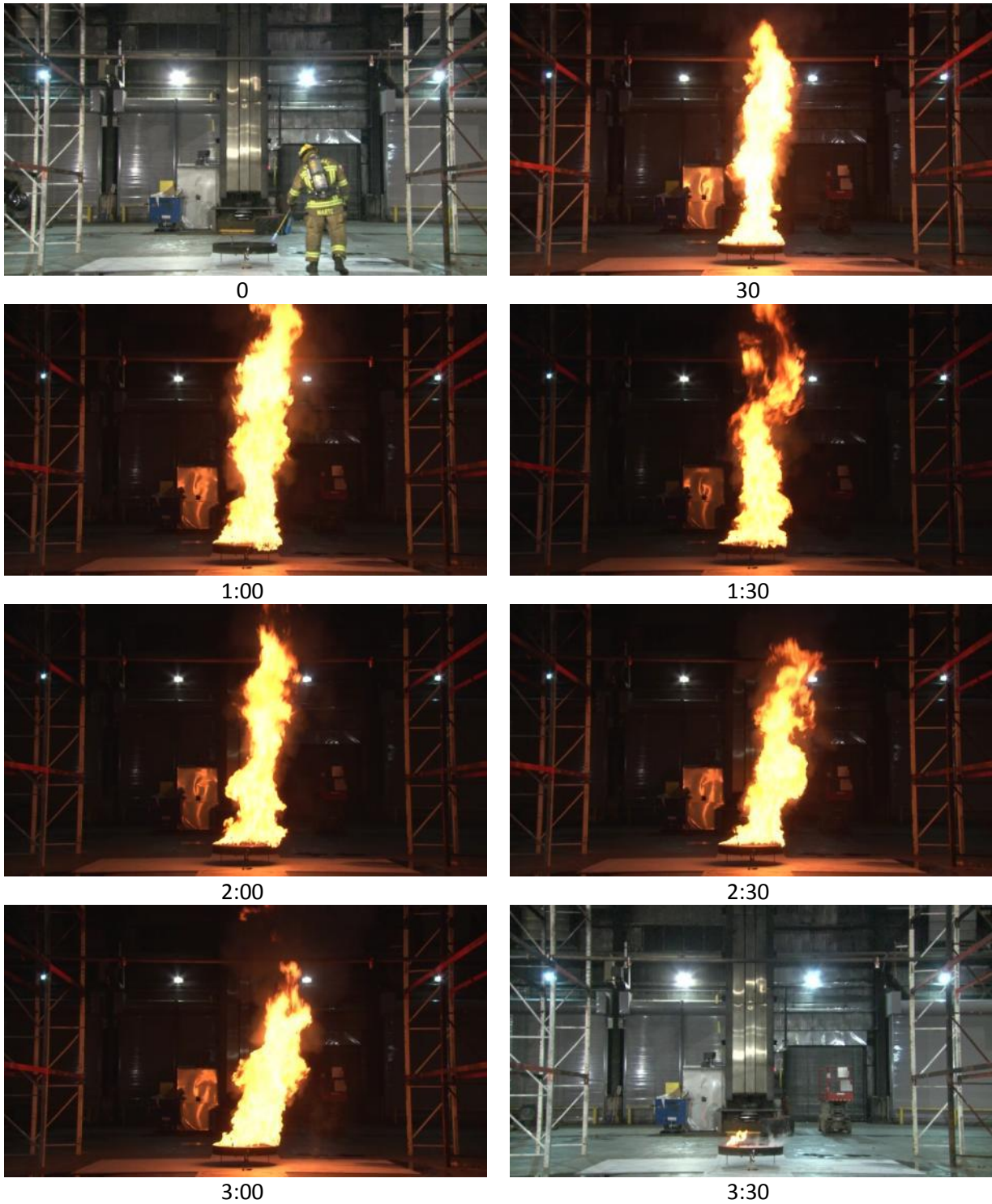
Figure   A-1: Selected frames from the side-by side demonstration test taken at 30 second intervals during Test 1.
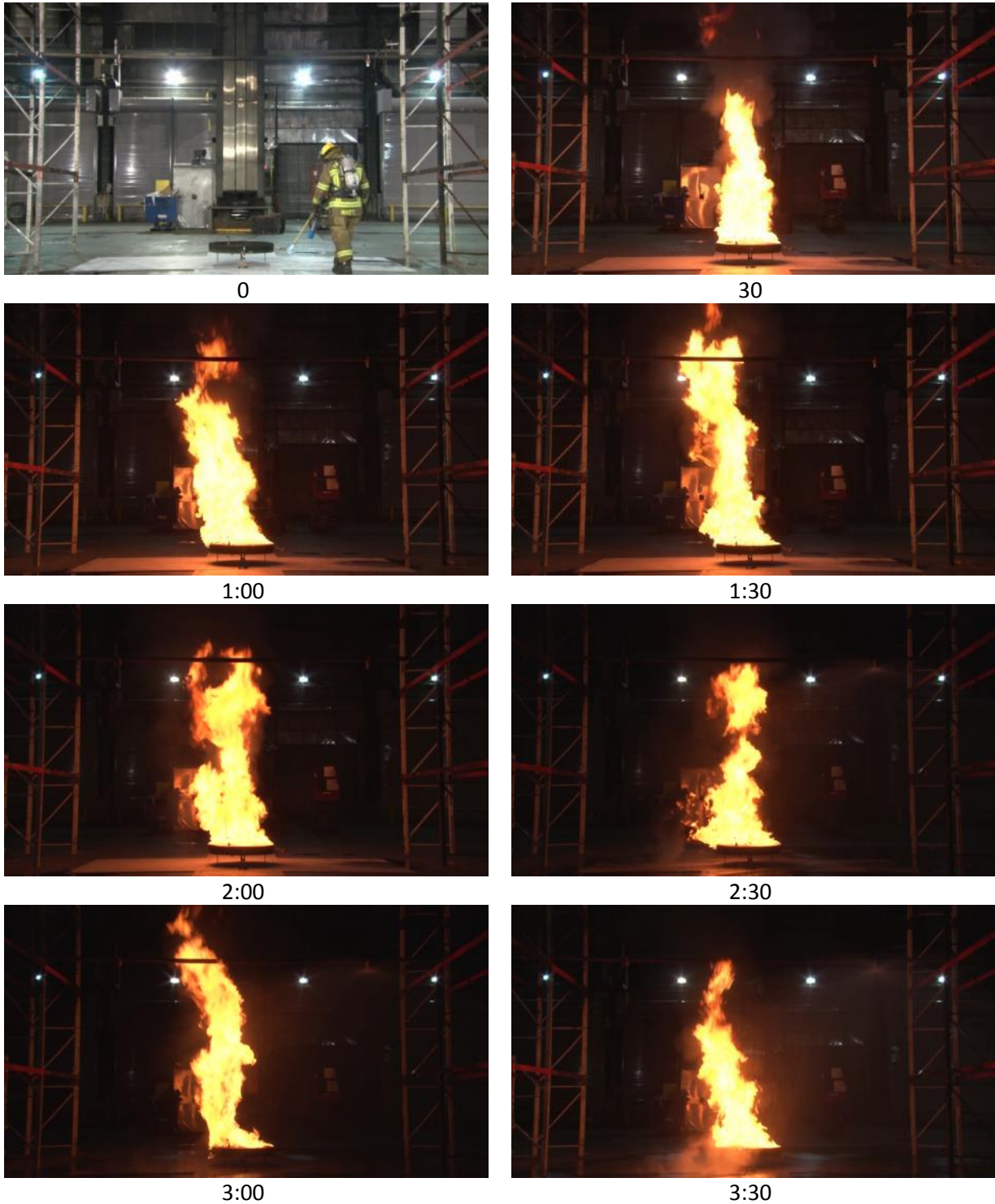
Figure   A-2: Selected frames from the side-by side demonstration test taken at 30 second intervals during Test 2.

0	30
1:00	1:30
2:00	2:30
3:00	3:30
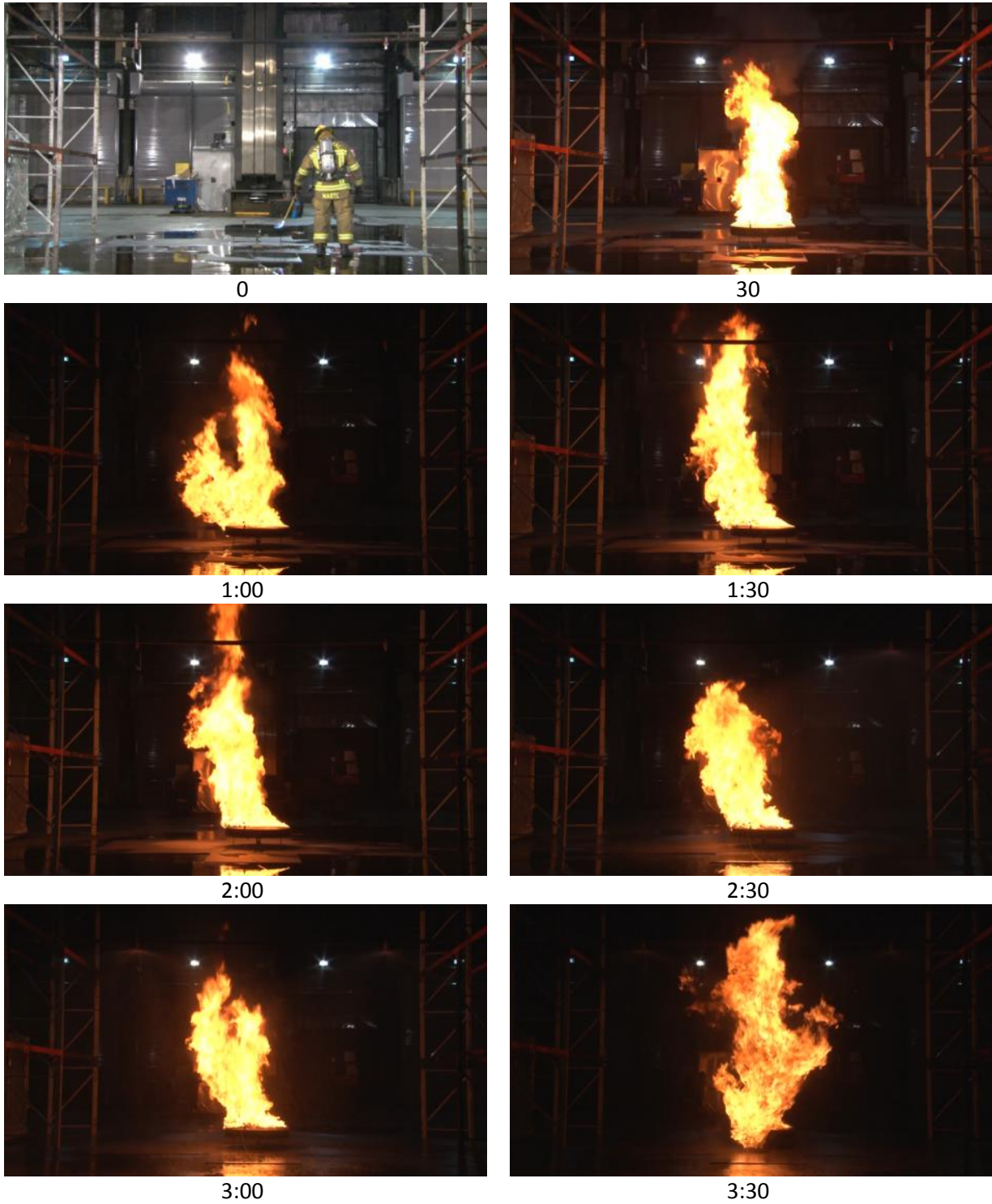
Figure   A-3: Selected frames from the side-by side demonstration test taken at 30 second intervals during Test 3.
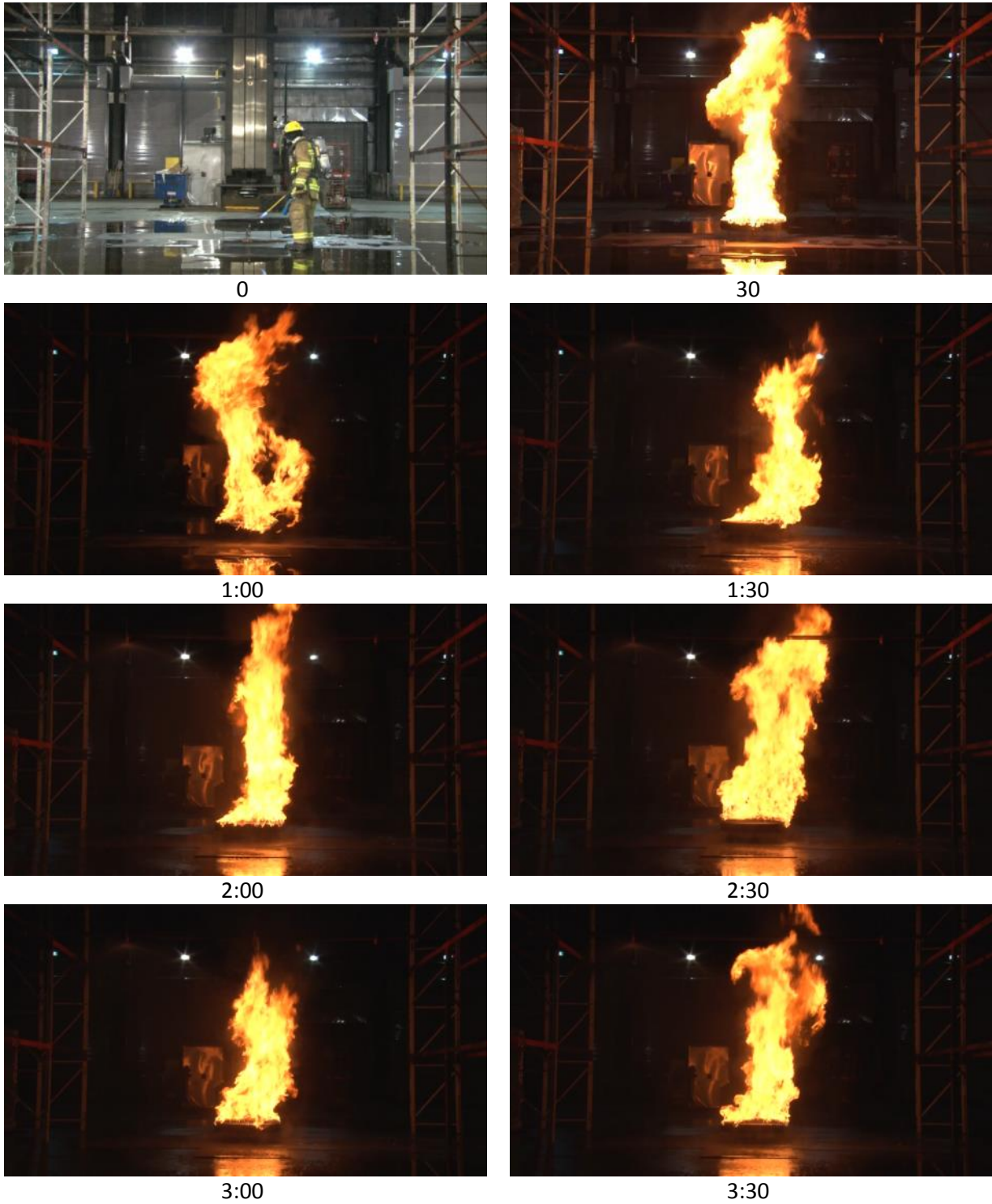
Figure   A-4: Selected frames from the side-by side demonstration test taken at 30 second intervals during Test 4.

0

30

1:00

1:30

2:00

2:30

3:00
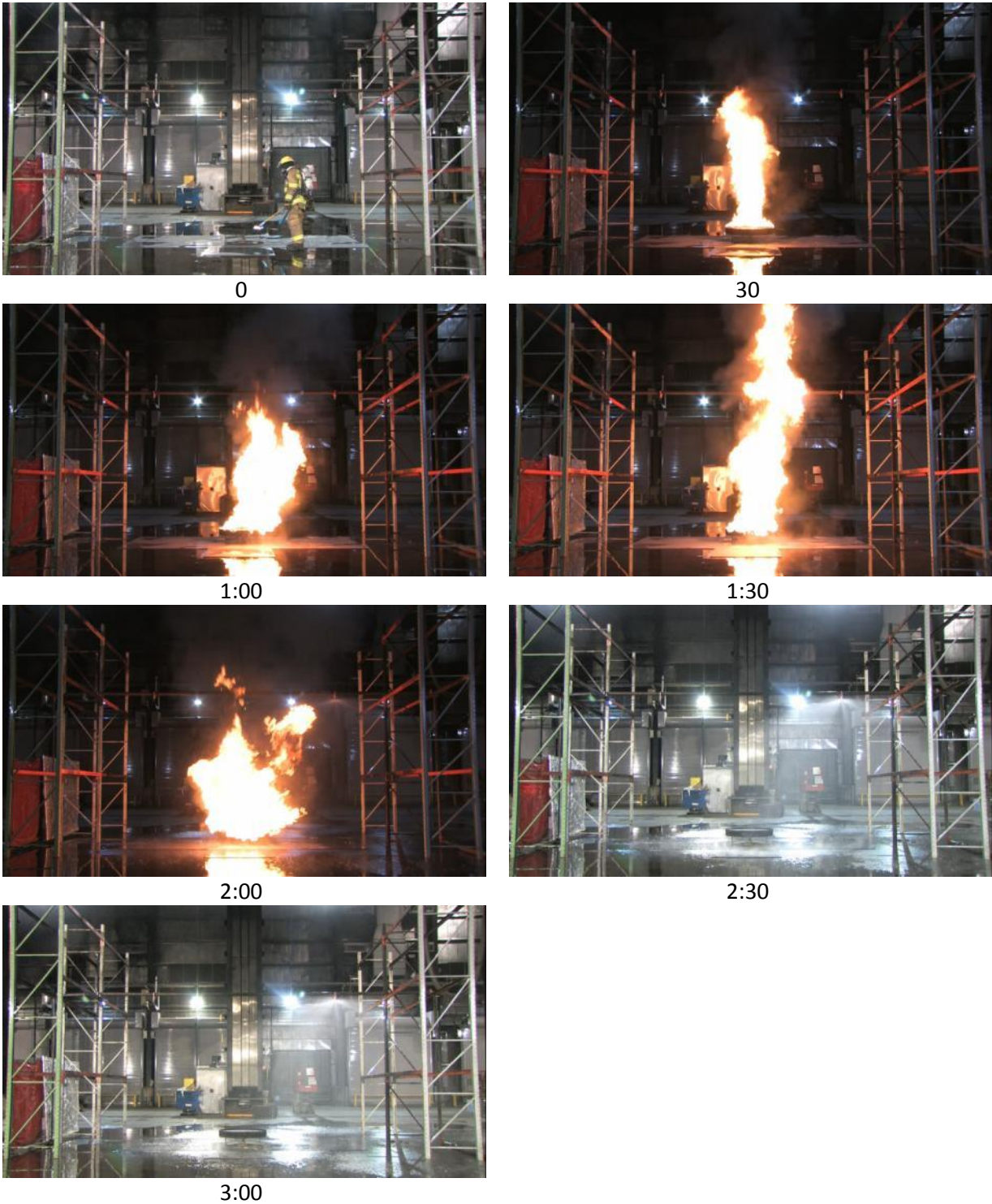
Figure   A-5: Selected frames from the side-by side demonstration test taken at 30 second intervals during Test 5.
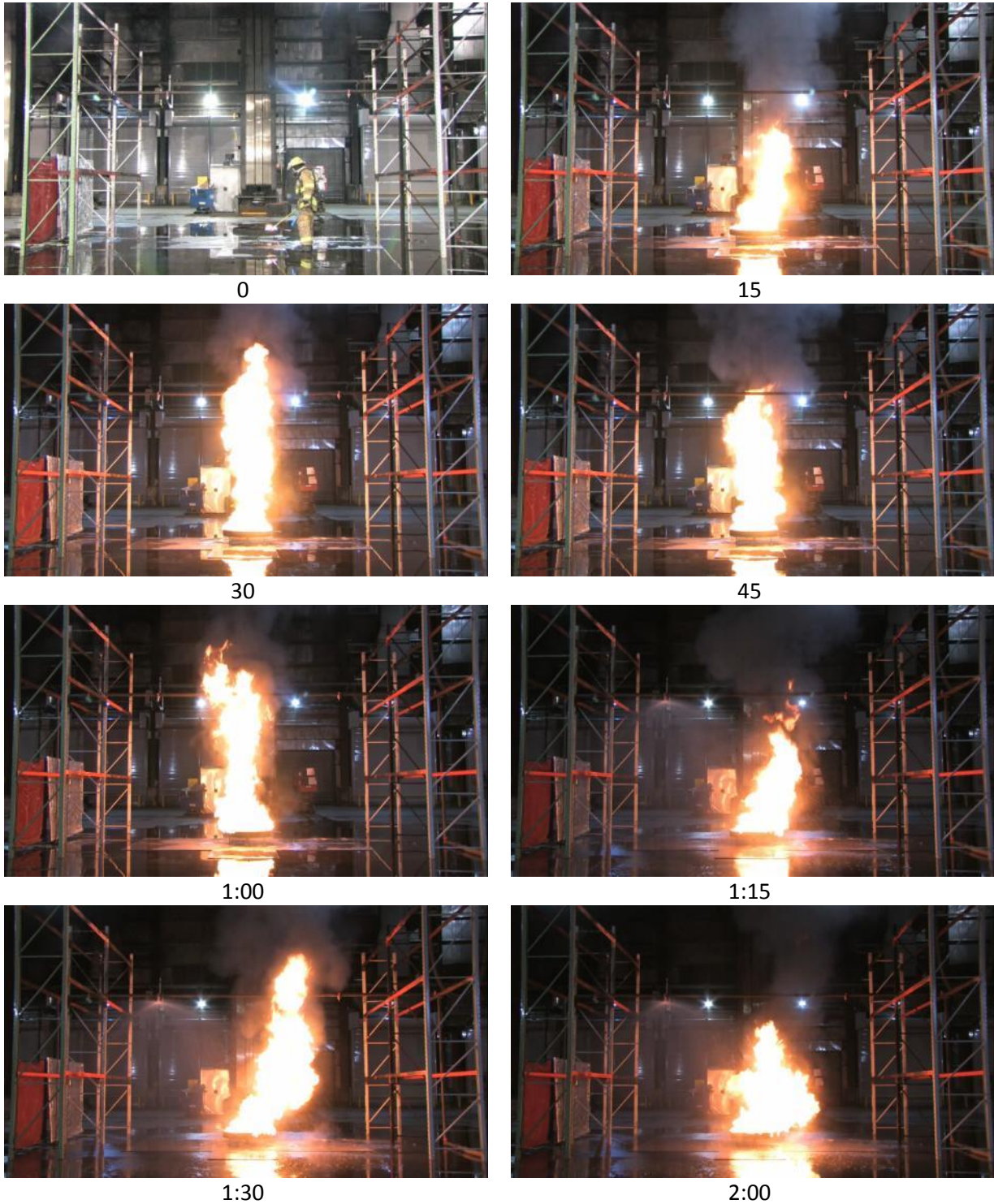
Figure   A-6: Selected frames from the side-by side demonstration test taken at 30 second intervals during Test 6.

0	30
1:00	1:30
2:00	2:30
3:00	3:30
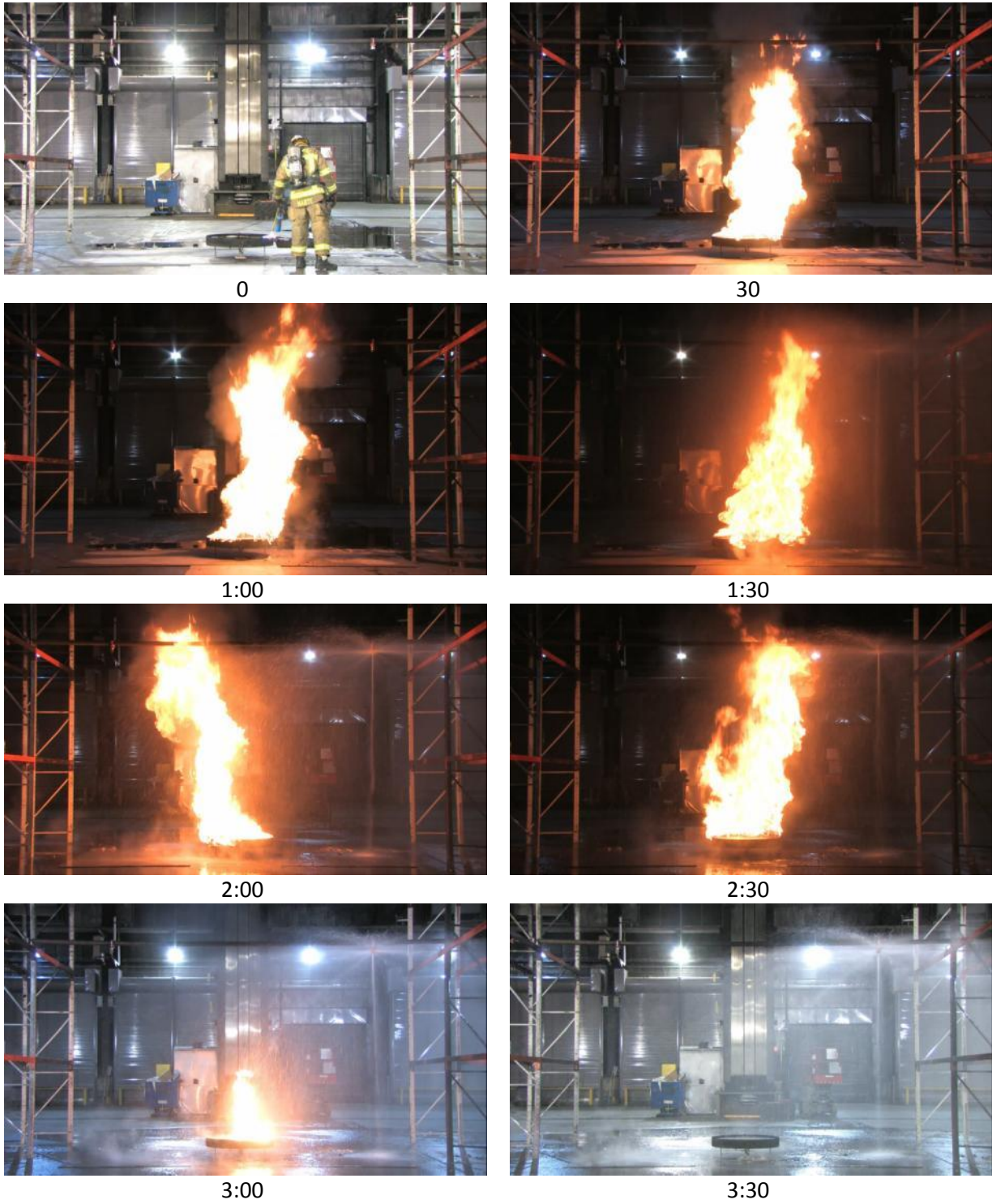
Figure   A-7: Selected frames from the side-by side demonstration test taken at 30 second intervals during Test 7.

0	30
1:00	1:30
2:00	2:30
3:00	3:30
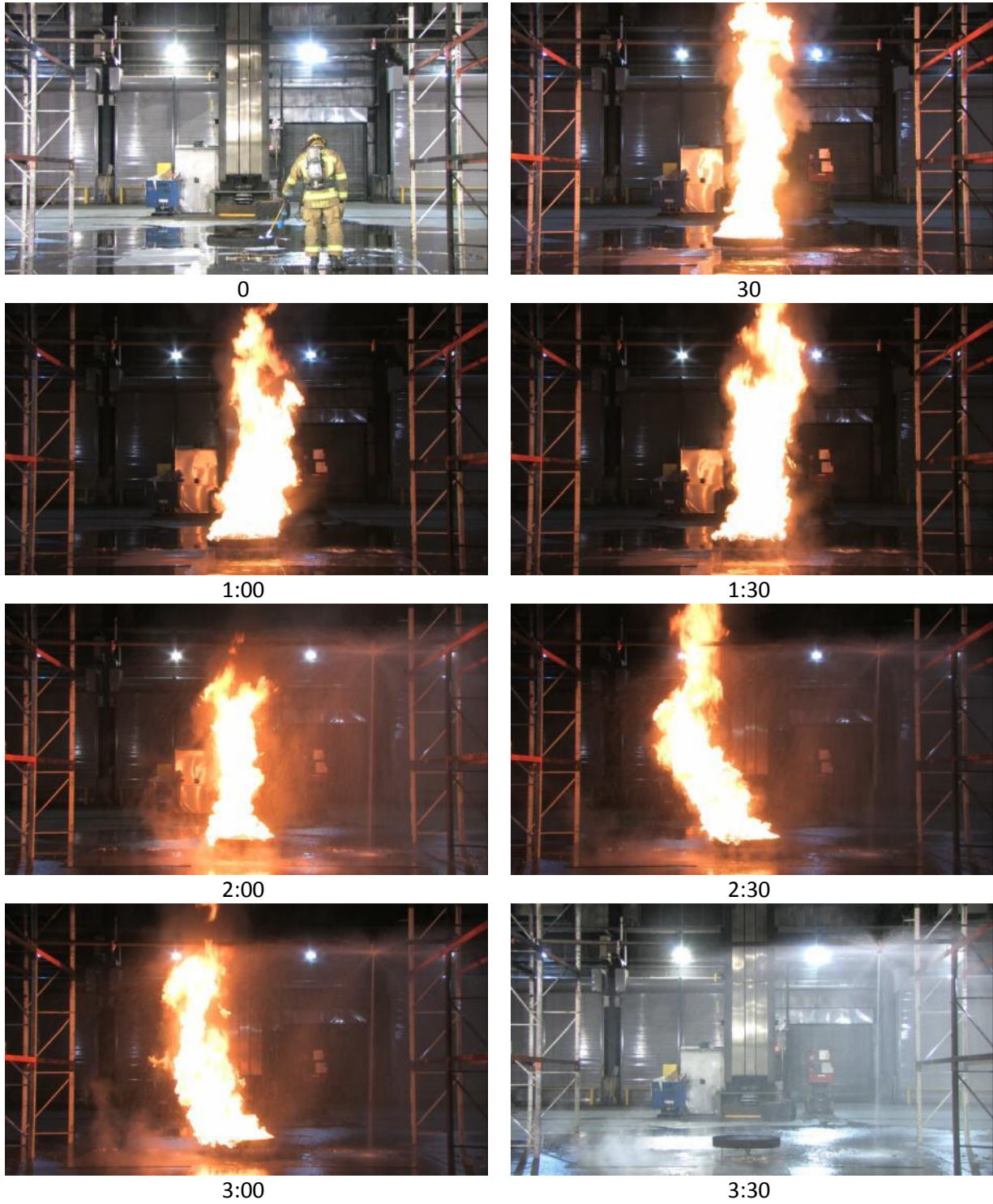
Figure   A-8: Selected frames from the side-by side demonstration test taken at 30 second intervals during Test 8.

| 0 | 30 |

| 1:00 | 1:30 |

| 2:00 | 2:30 |

| 3:00 | 3:30 |
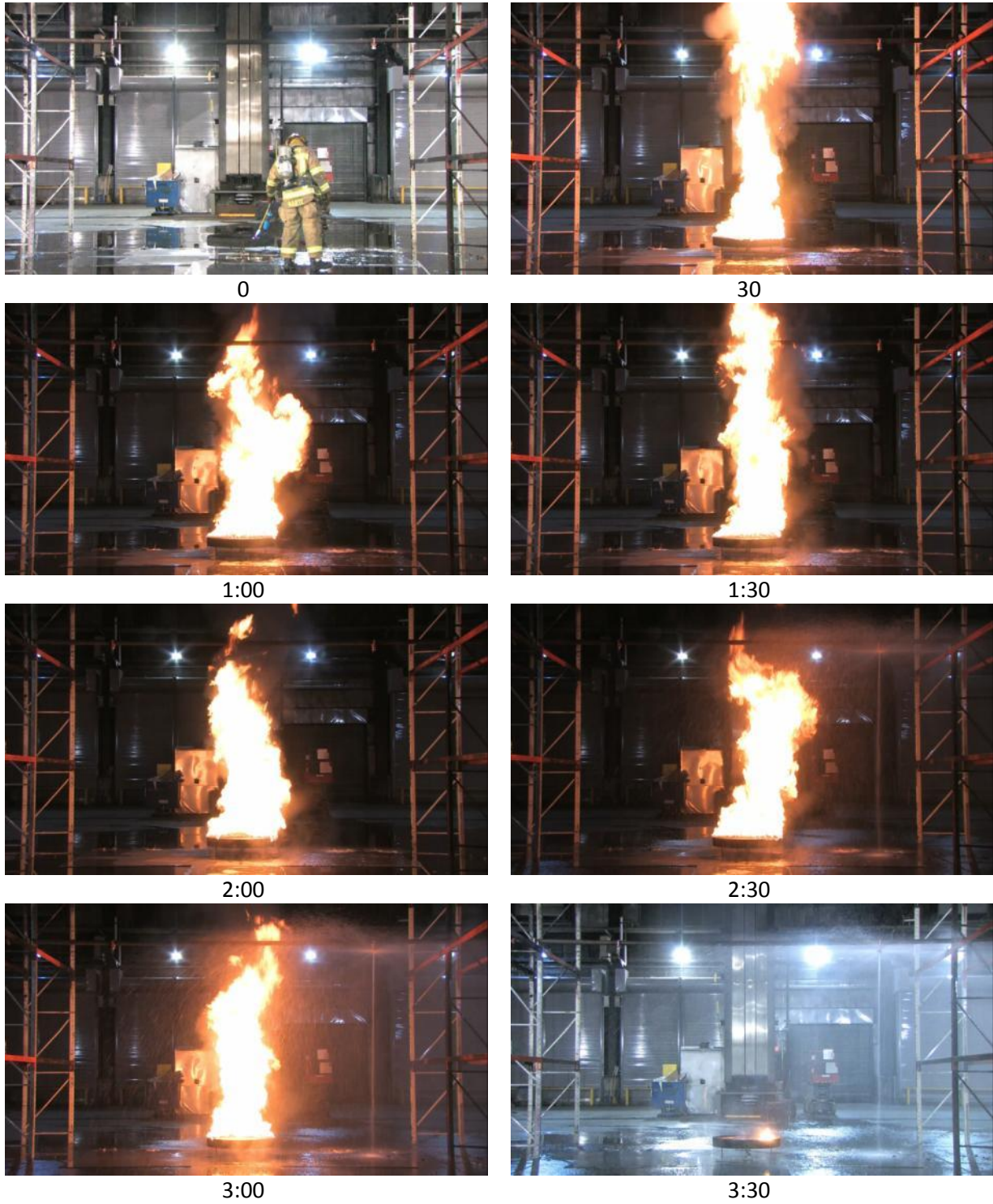
Figure   A-9: Selected frames from the side-by side demonstration test taken at 30 second intervals during Test 9.

0

30

1:00

1:30

2:00

2:30

3:00
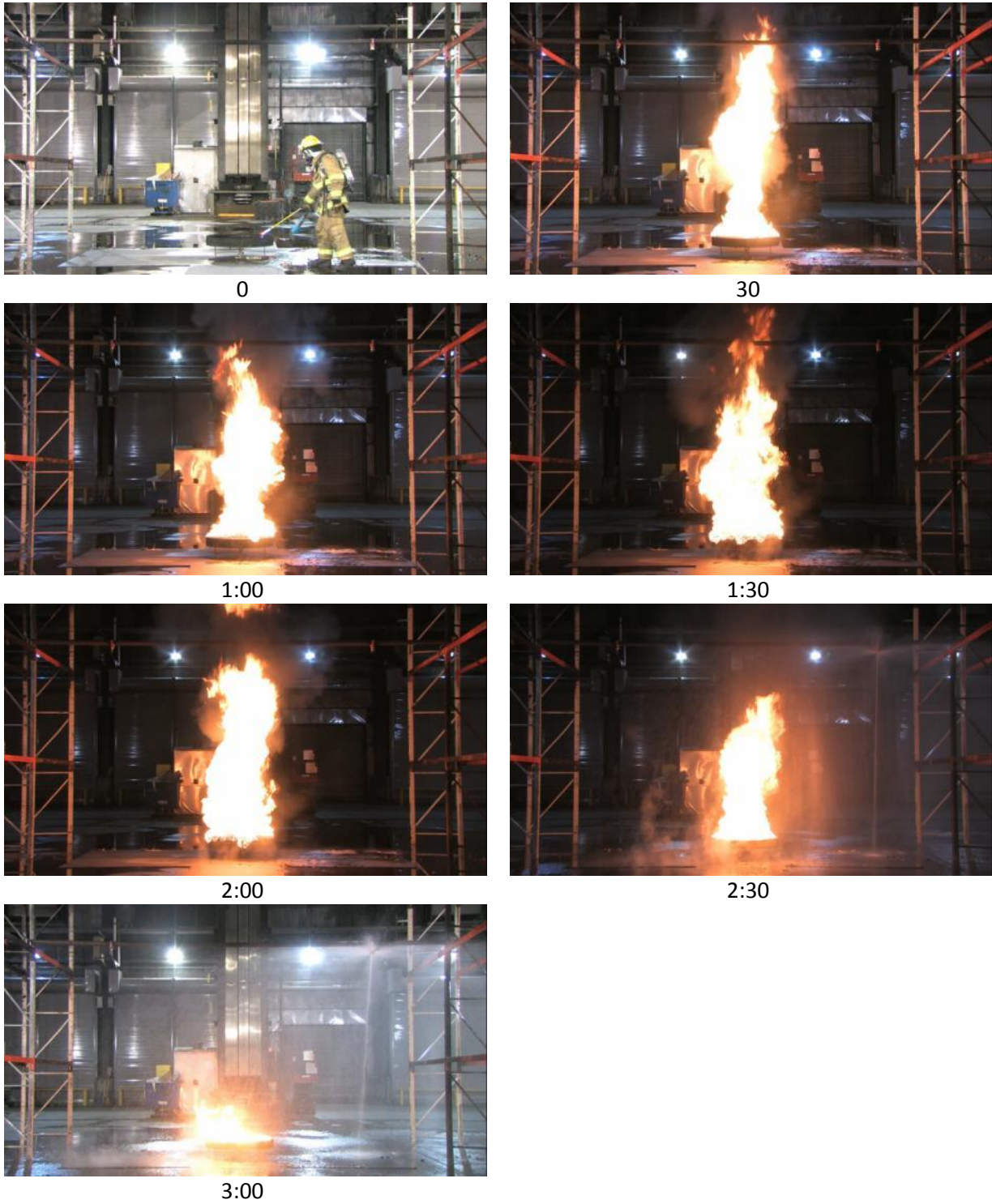
Figure   A-10: Selected frames from the side-by side demonstration test taken at 30 second intervals during Test 10.

FM Global®